Alma Mater Studiorum · Università di Bologna

Scuola di Scienze
Dipartimento di Fisica e Astronomia
Corso di Laurea Magistrale in Fisica

Advanced characterization of fired passivating contacts for silicon solar cells

Relatore:
Prof.ssa Daniela Cavalcoli

Correlatore:
Dott. Andrea Ingenito

Presentata da:
Sofia Libraro

Anno Accademico 2018/2019

Advanced characterization of fired passivating contacts for silicon solar cells

Sofia Libraro

Abstract

English version

Poly-crystalline Silicon based passivating contacts allow to reach high conversion efficiencies in silicon solar cells while being compatible with high temperature industrial processes. Among them, the fired passivating contact (FPC) approach allows easier integration with already existent production strategies, as it exploits the firing process, currently used by silicon industry for metallization of the cells, to achieve the formation of the junction.

The work presented in this thesis has been carried out in agreement between the Semiconductor Physics Group at the Physics and Astronomy Department of the University of Bologna, Italy, and the PV-Lab at École polytechnique fédérale de Lausanne (EPFL), Switzerland. The aim of the work is to provide insight into the working principles of fired passivating contacts (FPC) and to understand the mechanisms that control electronic transport in this kind of devices.

The performed experiments were carried out both on test samples and on solar cells containing the passivating layers. The used techniques allowed investigation of the passivation quality of the layers (photoluminescence imaging, PLI and quasi-steady-state photoconductance, QSSPC) and of their electrical transport properties, by transmission line measurements (TLM) and current-voltage (I-V) measurements on solar cells. Moreover, optical properties of the layers were investigated by means of surface photovoltage spectroscopy (SPV), Fourier-transform infrared spectroscopy (FTIR), spectral ellipsometry and Raman spectroscopy.

The main results include the identification of the optimal fabrication conditions (firing temperature and dwell time) of these kind of layer and the study of the evolution of the layer properties with different fabrication conditions. Two different electrical transport mechanisms were observed to take place in the FPCs, and the conditions in which one prevails over the other were individuated.

Moreover, transport in solar cells was investigated and the influence of the FPC layer properties on solar cells operation was studied.

Abstract

Versione italiana

I contatti passivanti basati sul silicio policristallino permettono di ottenere elevate efficienze di conversione e allo stesso tempo sono compatibili con i processi industriali ad alte temperature. Tra essi, l'approccio denominato *fired passivating contacts* (FPC) permette una semplice integrazione con gli attuali processi industriali, poiché la formazione della giunzione è basata sul processo di *firing*, già utilizzato dall'industria per la metallizzazione delle celle.

Il lavoro presentato in questa tesi è stato sviluppato in un progetto di collaborazione tra il gruppo di Fisica dei Semiconduttori al Dipartimento di Fisica e Astronomia dell'Università di Bologna e il PV-Lab della École polytechnique fédérale de Lausanne (EPFL), Svizzera. Lo scopo del lavoro è approfondire i principi di funzionamento dei *fired passivating contacts* e comprendere i meccanismi che controllano il trasporto elettronico in questo tipo di dispositivi.

Gli esperimenti sono stati condotti sia su campioni di prova sia su celle solari contenenti i contatti passivanti. Le tecniche utilizzate hanno permesso lo studio della qualità di passivazione dei *layers* (fotoluminescenza, PL, e *quasi-steady-state photoconductance*, QSSPC) e delle loro proprietà di trasporto elettronico tramite *transmission line measurements* (TLM) e misure di corrente-tensione (I-V) su celle solari. Inoltre, le proprietà ottiche dei campioni sono state studiate mediante spettroscopia di fototensione superficiale (SPV), spettroscopia infrarossa a trasformata di Fourier (FTIR), ellissometria e spettroscopia Raman.

I risultati principali includono l'identificazione delle ottimali condizioni di fabbricazione (temperatura e durata del *firing*) per questo tipo di campioni e lo studio dell'evoluzione delle loro proprietà con differenti condizioni di preparazione. Sono stati osservati due differenti meccanismi di trasporto elettronico nei FPCs, e sono state individuate le condizioni in cui uno prevale sull'altro.

Inoltre, è stato studiato il trasporto nelle celle solari e come le proprietà dei *passivating contacts* influenzino il funzionamento delle celle.

Contents

Introduction **1**

1 Generalities on solar cells **3**
1.1 Towards a renewable future . . . 3
1.2 The physics of solar cells . . . 7
1.2.1 Properties of sunlight . . . 7
1.2.2 Photovoltaic conversion . . . 8
1.2.3 Operational parameters . . . 11
1.2.4 Efficiency limit for a solar cell . . . 13
1.3 Three generations of solar cells . . . 15

2 Silicon solar cells **17**
2.1 State of the art . . . 17
2.1.1 Basic structure . . . 18
2.1.2 Screen printed diffused solar cells . . . 20
2.2 Surface and contact passivation . . . 23
2.2.1 Surface passivation mechanisms . . . 23
2.2.2 Passivating Contacts . . . 24
2.2.3 Fired Passivating Contacts . . . 26

3 Experimental methods **29**
3.1 Sample fabrication . . . 29
3.1.1 Plasma Enhanced Chemical Vapor Deposition . . . 30
3.2 Characterization techniques . . . 32
3.2.1 Surface photovoltage . . . 32
3.2.2 Photoluminescence imaging . . . 33
3.2.3 Quasi-steady-state photoconductance . . . 34
3.2.4 Raman Spectroscopy . . . 34

3.2.5 Transfer Length Measurements . . . 34
3.2.6 Optical Characterization . . . 37
3.2.7 I-V measurements on cells . . . 38

4 Results and discussion: layer optimization 41
4.1 First measurements on tunnel junction passivating layers: band diagram 41
4.1.1 Temperature dependent TLM . . . 43
4.1.2 Surface Photovoltage measurements . . . 46
4.1.3 Conclusions on SPV and TLM measurements . . . 51
4.2 Firing conditions optimization . . . 53
4.2.1 Raman spectroscopy . . . 53
4.2.2 Photoluminescence imaging . . . 54
4.2.3 Transport and passivation quality . . . 56
4.2.4 Temperature dependent TLM . . . 58
4.2.5 Optical measurements . . . 59
4.2.6 Conclusions on firing conditions optimization . . . 61
4.3 Importance of the firing . . . 63
4.3.1 Sample preparation . . . 63
4.3.2 Raman spectroscopy . . . 64
4.3.3 PL imaging . . . 65
4.3.4 QSSPC and TLM measurements . . . 65
4.3.5 Conclusions on silane variations . . . 67

5 Results and discussion: the role of passivating contacts in solar cells 69
5.1 Symmetrical samples . . . 69
5.1.1 Raman spectroscopy . . . 70
5.1.2 Quality of passivation . . . 71
5.1.3 Contact resistivity measurements . . . 72
5.1.4 Temperature dependent TLM . . . 74
5.1.5 Optical measurements . . . 74
5.1.6 Conclusions from analyses on symmetrical samples . . . 75
5.2 Solar cells . . . 77
5.2.1 Sample preparation . . . 77
5.2.2 Temperature dependent J-V . . . 78
5.3 General conclusions . . . 82

General conclusions and perspectives 85

Bibliography **88**

Appendix **93**

Introduction

In the framework of renewable energies, photovoltaic (PV) represents the fastest growing and more largely employed class of technologies [1]. In the recent years, huge progress has been made in the conversion efficiency of crystalline silicon solar cells, that account for 90% of PV market; these cells have now reached an efficiency grater than 26% thanks to the application of passivating contacts (PC) [2].

The key of high-performance PC is that the metal contacts are displaced from the semiconductor surface by inserting a thin (few nm) buffer layer aimed at passivating the silicon surface states by reducing the number of dangling bonds. In addition, these contacts also feature materials that provide charge carrier selectivity, inducing a potential at the c-Si surface that repels minority carriers and attracts majority ones [2].
These carrier selective contacts represent the ultimate solution to reach high conversion efficiency by suppressing recombination at the metal contact/semiconductor interface, that constitutes a major limiting factor to the performance of both laboratory scale and industrial solar cells [2].

Recently, passivating contacts based on poly-crystalline silicon (poly-Si) have attracted a lot of attention: they provide a high quality passivation, enabling to reach high conversion efficiency, and they are also compatible with high temperature industrial processes. These contacts consist in a thin (< 1.5 nm) oxide layer, that provides chemical passivation, on top of which a layer of doped poly-Si is deposited. In order to achieved the desired microstructural properties, the contacts have to go through a thermal annealing, that is usually done at high temperatures (> 800°C), and is slow (1-10°C/min ramps) and long (5-10 minutes) [4].
As an alternative approach, it has been demonstrated that it is possible to obtain passivating contacts with high quality also through a fast (50°C/s) thermal annealing, a firing. This approach has been termed *fired passivating contacts* (FPC) [5].

The aim of this work is to provide insight into the working principles of FPC, in particular to clarify the relation bewteen fabrication conditions and charge transport properties. The investigation has been carried out with a variety of experimental techniques in order to study electrical and optical properties of the passivating layers.

The structure of this thesis is the following: *Chapter 1* provides an introduction to photovoltaics, presenting the basic working principles of a solar cell and giving a brief overview over existing PV technologies. *Chapter 2* presents the state of the art in silicon solar cells and passivation technologies, introducing the concept of passivating contacts.
Chapter 3 is dedicated to the description of experimental techniques, both for characterization and sample preparation.
Finally, *Chapter 4* and *Chapter 5* are dedicated to the explaination and discussion of experimental results: the former chapter contains results relative to optimization of the preparation process, while the latter is dedicated to an analysis of the relation between the properties of passivating contacts and the working principles of solar cells containing them.
The final chapter gives some general conclusions and provides suggestions for futher developement of the topic.
The work is completed by an appendix containing all the acronyms that have been used in the thesis.

Chapter 1

Generalities on solar cells

1.1 Towards a renewable future

Earth's temperature is the result of a fragile equilibrium established between the incoming radiation from the sun and the energy radiated into space by Earth. The outgoing radiation emitted by the Earth is strongly affected by the presence and composition of the Earth's atmosphere; the most important atmospheric gases are nitrogen (N_2), oxygen (O_2), argon, with traces of other gases such as water vapour, carbon dioxide (CO_2), ozone and methane. A natural background level of 270 ppm carbon dioxide in the atmosphere absorbs outgoing radiation, thereby keeping this energy in the atmosphere and warming the Earth. Outgoing radiation is strongly absorbed by carbon dioxide in the 13-19 μm wavelength band and by water vapour in the 4-7 μm wavelength band. Most outgoing radiation (70%) escapes in the window between 7-13 μm, but the remaining 30% of it does not leave the atmosphere. This phenomenon, known since the 1820s, is called greenhouse effect; it contributes to keep the planet much warmer than it would be without an atmosphere [6].
Human activities are increasingly releasing anthropogenic gases, such as carbon dioxide, methane and nitrous oxides, into the atmosphere. These gases, known as greenhouse gases or GHG, absorb in the 7-13 μm range, therefore preventing the normal escape of energy and leading to an increase in the terrestrial temperature.

According to the last published report of the Intergovernmental Panel for Climate Change (IPCC), the last 30 years were *likely* the warmest period of the last thousand years in Northen Emisphere [7].
Figure 1.1 shows data relative to GHG concentration in the atmosphere and some of their effects: land and ocean surface temperature anomaly and change in sea level. An

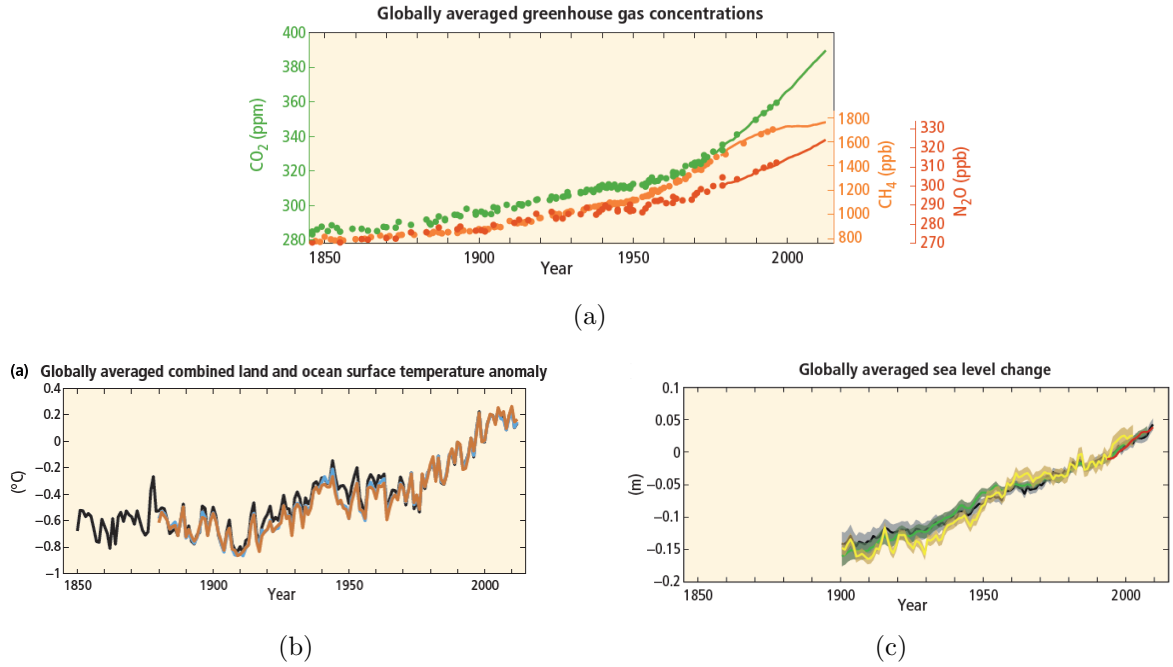

Figure 1.1: Indicators of climate change over the last $\sim$ 150 years: (a) greenhouse gases concentration in the atmosphere, (b) globally averaged land and ocean surface temperature anomaly and (c) globally average sea level change. [7].

increasing trend is clearly visible over the considered period, suggesting a correlation between increase in GHG emission and changes in the climate system. IPCC concludes that the effect of the human influence is *extremely likely* to have been the dominant cause of the observed warming since mid-20th century [7].
We are already witnessing the effects of GHG emission, but these effects will become more and more dramatic in the future. Projections of current trends over the next 80 years are not at all encouraging: as an example, Figure 1.2 shows the average change in surface temperature over the end of the 20th century, compared with a multi-model projection for the end of the 21st century [7].

To prevent this dramatic scenario from becoming reality, it is necessary to drastically reduce GHG emission in the near future. Figure 1.3 shows the contributions to CO_2 emission by human activity. It is clear that the most important one comes from burning of fossil fuels and other industrial activities, which account for the 70% of the total. With the Paris Agreement in 2016, the United Nations have agreed to the goal of holding the average temperature increase below 2 °C. This is a first step towards the application

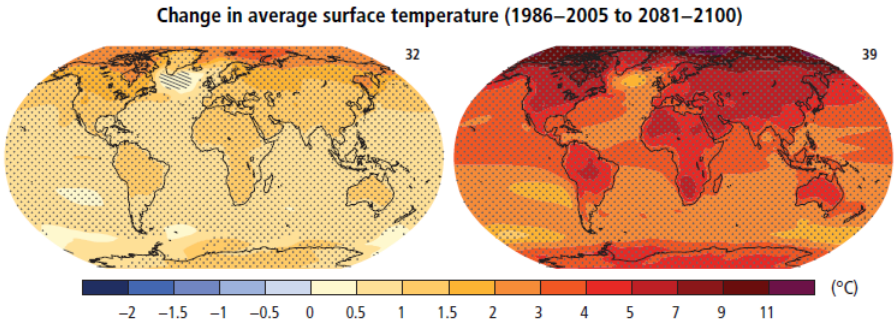

Figure 1.2: Comparison in changes of land and ocean surface temperature between 1986-2005 and 2081-2100 [7].

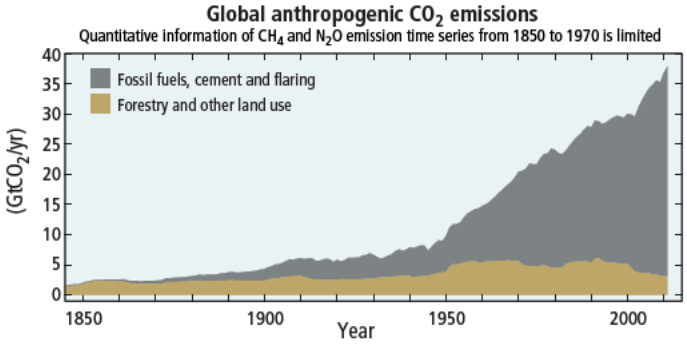

Figure 1.3: CO_2 emission from human activities [7].

of strategies to reduce GHG emission, adopt sustainable policies and setting targets to mitigate climate change [8].

Within this context, it is clear that the current most common methods of producing electrity, that is, exploiting fossil fuels, are no longer sustainable. Over the last years, more and more efforts have been put in research to develope energy sources that could allow the transition to a low-carbon economy as soon as possible.
In the present day, majority of the global energy supply is still provided by fossil fuel; as shown in Figure 1.4, oil, natural gas and coal still account for 87% of the total power supply. Renewable energies are about to reach 10% of the overall share and represent a growing sector, with energy efficiency improvement and more and more penetration in the electricity sector [9].

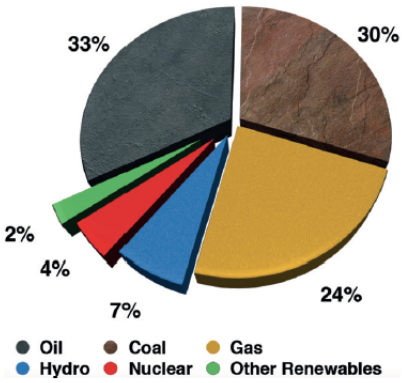

Figure 1.4: Global supply of primary energy, 2015 [9].

Between renewable energies, solar photovoltaics (PV) is the technology that has shown fastest growth over the last few years. Continuously falling prices and improving energy efficiency are making PV one of the lowest cost options for future electricity supply. It has been estimated that, at this rate, by 2030, 35% of the additional electricity generation capacity installed will be provided by PV [10].
Sunlight can be regared as the ultimate energy source: it is abundant, inexhaustible and fairly homogeneously distributed over Earth's surface. In 2014, the global energy consumption rate was 17.4 TW, which is almost four orders of magnitude smaller than the solar energy irradiating the planet [9].
Of course, solar energy must be converted into *usable* energy forms, such as heat, fuels or electricity; this creates both theoretical (conversion efficiency limitations due to the nature of the processes) and technical problems, that limit the possibility of using solar energy in everyday life [9]. The achievement of high power conversion efficieny and long term reliability, as well as the reduction of manufacturing costs, are the main challenges for large scale production of PV modules and to ensure that solar energy becomes increasingly competitive in the global market of energy resources.

1.2 The physics of solar cells

1.2.1 Properties of sunlight

The sun radiates energy into space in the form of photons, that cover a wide energetic spectrum. The power spectrum of the sun can be approximated by the radiation of a blackbody at ∼5800 K, as shown by the black line in Figure 1.5. The real spectrum of radiation as received on Earth, however, does not have this simple form: the power at sea level depends on the geographical location, season and night and day cicle, and absorption and scattering of light by the atmosphere.
In order to quantify the effects of the atmosphere it is useful to introduce the concept of air mass (AM): it is defined as the optical path of sunlight through Earth's atmosphere normalized to the thickness of the atmosphere. AM1 corresponds to the sun at zenith; as a convention, it is agreed that the power of the sun is equal to 1kW/m^2 at AM1.5, which correspond to an angle of 48.2 °[11].
AM0 corresponds at the top of the atmosphere. Figure 1.5 shows the sun spectrum corresponding to AM0 and AM1.5.

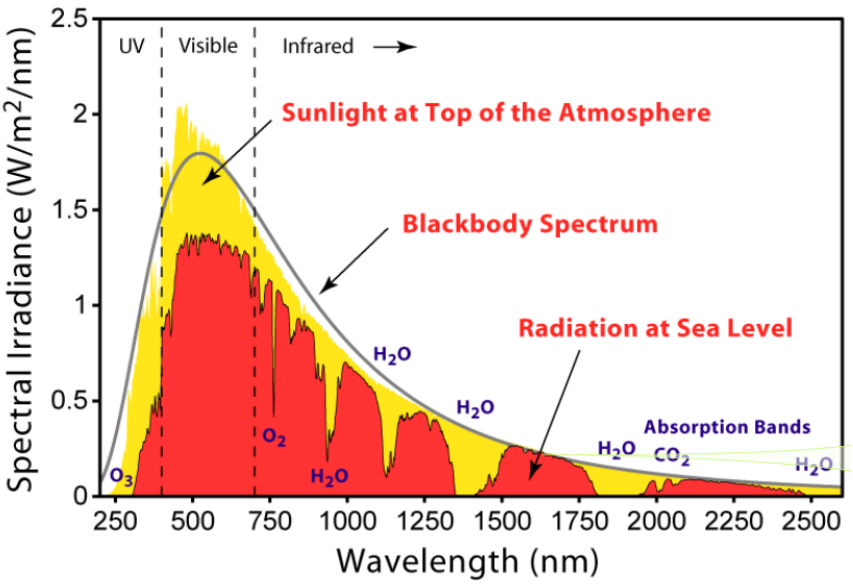

Figure 1.5: Specrtal irradiance as a function of wavelength of solar radiation. The radiation of a blackbody (ideal behaviour) is compared with the actual sun spectrum at the top of the atmosphere (AM0) and at sea levels (AM1.5) [12].

In order to exploit the energy coming from the sun, it is necessary to convert it into electric power; this means generating a photocurrent (creation of mobile charge carriers by light absorption) and a photovoltage (a potential difference given by charge separation). These are the fundamental functions of a solar cell.

1.2.2 Photovoltaic conversion

Basic structure of a solar cell

A solar cell is essentially formed by a p-n junction with electric contacts at its ends. When a photon coming from the sun impinges on the junction, it may generate electron-hole pairs, thus producing electric current. These electron-hole pairs are then separated by the voltage present across the junction (which may be internal or applied from the outside) and collected at the contacts. A scheme that illustrates how a solar cell works is shown in Figure 1.6.

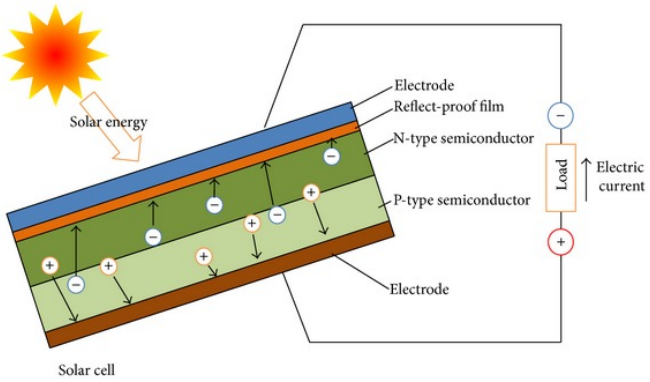

Figure 1.6: Schematic view of a solar cell [6].

The effect of the photon on the junction depends on its energy E_γ and on the bandgap E_g. Two cases are possible:

- If $E_\gamma < E_g$, nothing happens;
- If $E_\gamma \geq E_g$, the photon will generate an electron-hole pair.

It is important to note that a photon with energy $E_\gamma >> E_g$ will have the same effect as a photon with energy just above the bandgap; the excess energy is lost.

Light generated current

From the above discussion, it appears clear that in order to have a high quality solar cell, which efficiently converts sunlight into electric power, a material whose bandgap matches the sun spectrum (Figure 1.5) is needed. Moreover, the created electron and hole pairs must be able to travel through the cell without recombining in order to be collected at the electrodes. The presence of a p-n junction prevents recombination of carriers by separating them through the electric field created at the junction.

Not all generetaed carriers are able to be separated by the p-n junction; the collection probability describes the probability that a carrier generated in a certain region of the device will be collected by the junction and contribute to the photo-current [6]. Collection probability depends on the position in the cell where the carrier is created, on the diffusion length of the carrier and on surface properties of the device. The collection probability is high in the depletion region and nearby, but it decreases as the carriers are generated further away from the junction. A carrier generated more than a diffusion length from the junction will have a very low collection probability. Surfaces are also problematic regions in terms of collection probability, as they tend to have a higher density of defects than the bulk of a material; defects act as recombination centres, making the collection probability very low. Passivation of surface defects in order to prevent recombination is thus a key step in the production of a solar cell, as it allows to improve charge collection in the device, giving a higher light-generated current.

Light generated current depends both on collection probability ($CP(x)$) and on the carrier generation rate in the cell ($G(x)$); both these parameters depend on the spatial position x in the cell. The current is given by Equation 1.1:

$$J_L = q \int_0^W G(x) CP(x) dx \tag{1.1}$$

The photovoltaic effect

The generation of charge carriers does not necessarily imply a power generation in the cell; a voltage is needed as well. The generation of a voltage in a solar cell is known as *photovoltaic effect* [6].
As charge carriers are generated by light absorption, they are separated by the field in the p-n junction; this causes the shift of electrons on the n-doped side and of holes on the p-doped side of the junction. If the carriers are prevented from leaving the junc-

tion (open-circuit conditions), charge accumulation occurs. This separation of charge creates an electric field that is opposite to the one already present in the junction; the total electric field is therefore reduced by the effect of light irradiation. As the electric field represents a barrier to carrier diffusion across the junction, the diffusion current increases, establishing an equilibrium between diffusion current and light generated current. The difference between those is the total current from the solar cell.

I-V characteristic of a solar cell

As the solar cell is basically formed by a p-n junction, its I-V curve when not illumnated is the same as a diode. The curve under illumnation conditions is the superposition of the diode's I-V in the dark and the light generated current; the final expression in the first quadrant is given by Equation 1.2:

$$I = I_L - I_0[\exp(\frac{qV}{nkT})] \tag{1.2}$$

where I_0 is the diode saturation current density and I_L is the light generated current. Plotting 1.2 gives the red curve shown in Figure 1.7. The blue line in Figure shows the electric power produced by the cell, $P_{el} = I \cdot V$.

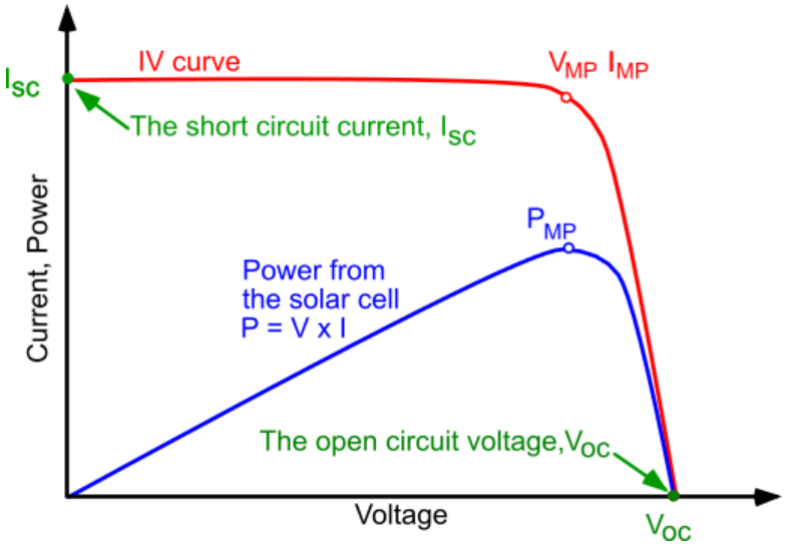

Figure 1.7: I-V curve of a solar cell under illumination (red curve). The power as a function of the voltage is also plotted (blue curve). Operational parameters I_{SC} and V_{OC} are indicated in green [6].

1.2.3 Operational parameters

An illuminated solar cell can be represented as a battery in a circuit: it can provide a certain photovoltage at a given photocurrent. The photocurrent comes from electron-hole pair generation and collection at the electrodes. The photovoltage is the potential difference between the contacts, which is necessary in order to prevent charge separation and can be either intrinsic (coming from the p-n junction itself) or applied from the outside [11].

A certain point on the I-V of a cell, the red line plotted in Figure 1.7, corresponding to a specific combination of I and V values, is called a working point (red dot in Figure). A working point can be fixed by choosing a load resistance R_L, so that

$$R_L = \frac{V}{I} \tag{1.3}$$

Rather than with the working point, it is more convenient to describe a solar cell's performance with other parameters which will be described in the following.

Open circuit voltage and short circuit current

The open circuit voltage V_{OC} is the voltage present between the electrodes of the cell in open circuit conditions. In this case the load resistance is infinite, and the current is I=0. When the terminals are closed, the cell is in short circuit condition. In this case the fundamental parameter is the open circuit current I_{SC}, the current flowing in the cell when V=0 and $R_L = 0$ [11].
These parameters are highlighted in green in Figure 1.7.

Open-circuit voltage is the maximum voltage that can be obtained from a solar cell. An expression for it can be found by setting $I = 0$ in Eq. 1.2:

$$V_{OC} = \frac{nkT}{q} \cdot \ln(\frac{I_L}{I_0} - 1) \tag{1.4}$$

Equation 1.4 shows that V_{OC} depends on the light generated current and the saturation current. The latter has the greatest influence on V_{OC}; since I_0 depends on the amount of recombination in the solar cell, measuring the open-circuit voltage allows to quantify the effects of the recombination in the device, giving an idea of the passivation quality of the cell [11].

The short circuit current depends on the generation and collection of charge carriers. For an ideal solar cell, with minimum resistive losses, I_{SC} is equal to the light generated current. In a real solar cell, resistive losses are not neglectable, it is always $I_L < I_{SC}$. The short-circuit current thus represents the maximum current obtainable from a cell [11].

Maximum power point and Fill factor

There is one combination of values of I and V that yields the maximum output power. These values correspond to a point on the I-V characterstic that is called the maximum power point (shown by the blue dot in Figure 1.7):

$$P_{mpp} = I_{mp} \cdot V_{mp} \tag{1.5}$$

Having introduced these quantities, a new parameter can be defined. The fill factor (FF) is defined as

$$FF = \frac{I_{mp} \cdot V_{mp}}{I_{SC} \cdot V_{OC}} \tag{1.6}$$

Graphically, the fill factor represents the ratio between the area of the purple rectangle and the pink one in Figure 1.8, and is usually one of the parameters used to describe a solar cell, as it allows to describe the maximum power, current and voltage obtainable from a cell [11].

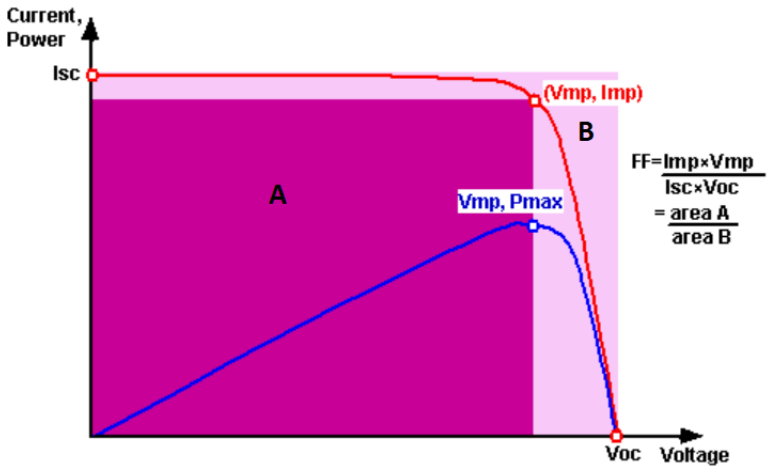

Figure 1.8: Graphical interpretation of the fill factor of a solar cell. [6].

Solar energy conversion efficiency

The solar energy conversion efficiency, η, describes how well the cell is able to convert sunlight into electric power. It is the ratio bewteen the output maximum power and the input power coming from the sun. A convenient way to define it is by using the fill factor:

$$\eta = \frac{P_{mpp}}{P_{sun}} = FF \cdot \frac{I_{SC} \cdot V_{OC}}{P_{sun}} \tag{1.7}$$

The efficiency describes the performance of a solar cell itself, but it also depends on external factors such as intensity and spectrum of the incident light and the temperature. In order to compare different cells, the same external conditions must be reproduced. Solar cells operating on Earth are usually tested at the so-called *standard test conditions* (STC), with T=25°C and AM1.5 [6].

1.2.4 Efficiency limit for a solar cell

What is the maximum energy conversion efficiency that can be obtained from a solar cell? In principle, sunlight can be converted into electricity with an efficiency that is close to the Carnot limit, that can be calculated with a thermodynamic approach, of 95% [14]. This limit, however, is not realistic and does not describe real devices. A more realistic approach uses the detailed-balance principle and allows to calculate the maximum efficiency for a single-junction solar cell under non-concentrated light; in this way the so-called Shockley-Queisser limit can be obtained.
The SQ limit describes the maximum efficiency of a single junction solar cell working with non-concentrated light, at AM1.5, and is based on several assumptions [13]:

- The only recombination process that is present, which brings a decrease in the generated photocurrent, is radiative recombination;
- The splitting of the quasi-fermi level is constant throughout the cell, that is, the mobility is infinite. This means that carriers are always collected, no mattere where they are generated;
- All photons with $E > E_g$ are absorbed;
- Each photon generates one electron-hole pair.

Shockley and Queisser's approach is based on calculating the net absorbed photon flux, as a difference between the radiation absorbed both from the sun and Earth and the radiant emission flux [13].

The efficiency obtained within this approach is bandgap-dependent, as shown in Figure 1.9. The maximum value of efficiency, for $E_g \sim 1.5$, is $\eta \sim 0.31$.
If the hypotheses of the detailed balance approach hold, this limit cannot be overcome. Figure 1.9 shows the theoretical limit (green line) calculated by Shockley and Queisser and real efficiencies for AM1.5 and AM0; real efficiencies are lower than the theoretical limit because non-radiative recombination and resistive losses, that are neglected in the calculation.

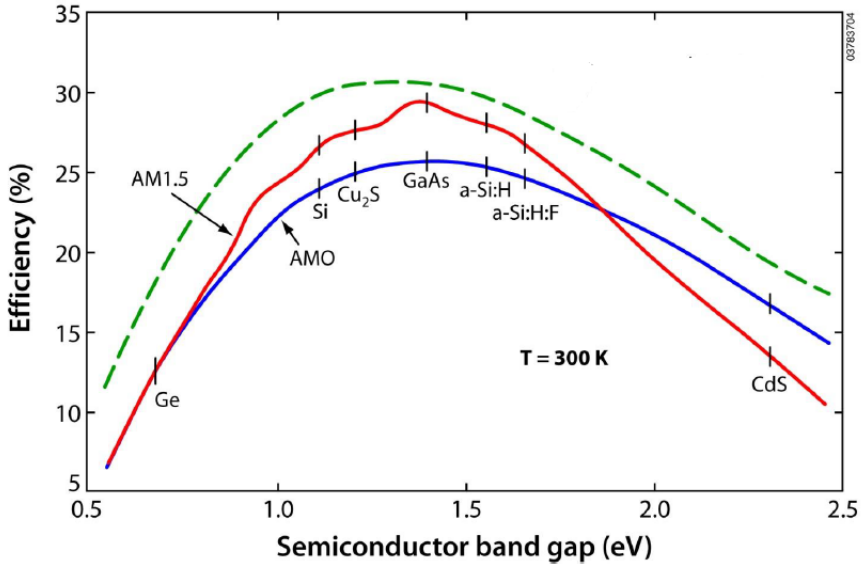

Figure 1.9: Solar cell efficiency vs bandgap for an ideal cell (green) and for real cells at AM1.5 (red) and AM0 (blue) [6].

1.3 Three generations of solar cells

The first practical photovoltaic device was demonstrated in the 1950s but, for a long period after that, PV was never considered as a real alternative to fossil fuels, remaining confined to application in the space industry. It was only with the oil-crisis in the 1970s that global attention was drown on the need for an alternative energy source; this promoted the investigation of PV as a means to generate power [6].
In the 1980s, research on silicon solar cells started to achieve memorable results, as the 20% conversion efficiency in 1985. A photovoltaic industry based on crystalline or polycrystalline silicon solar cells began to grow rapidly and to gain more and more importance as an alternative to fossil fuels [6].

PV based on silicon wafers, the so-called *first generation technology*, is still the most important in terms of global diffusion: in 2015, 90% of total PV production came from first generation solar cells [14]. The success of silicon is easily explainable: it is the second most-abundant material in the earth's crust, non-toxic and prices for fabrication of silicon PV are continuously falling [10].

A *second generation* of solar cells started to be studied in the 1980s: cells based on thin-film technology, both based on silicon (amorphous and thin film silicon) and other materials such as CdTe or CuInGaSe (CGIS). This kind of technology is promising, as it allows to cover large areas at low costs and to eliminate the cost of silicon wafers [14].

Both these generations are limited by the conversion efficiency limit at 31%, calculated for single-junction solar cells (see Section 1.2.4). Even though module efficiency is still very far from this result, it is reasonable to try and develope innovative technologies capable of overcoming this limit. This is the goal of the *third generation technology*, that aims at obtaining high performance cells at low costs [14]. A typical example of third generation technology is given by tandem solar cells, that are based on the presence of different materials with different bandgaps, therefore capable of absorbing in different regions of the sun spectrum. Making use of multiple junctions, these cells allow to overcome the Shockley-Queisser limit [14].

Figure 1.10 shows the most updated (2019) efficiency chart of PV solar cells by the National Renewable Energy Laboratory (NREL) in the US.

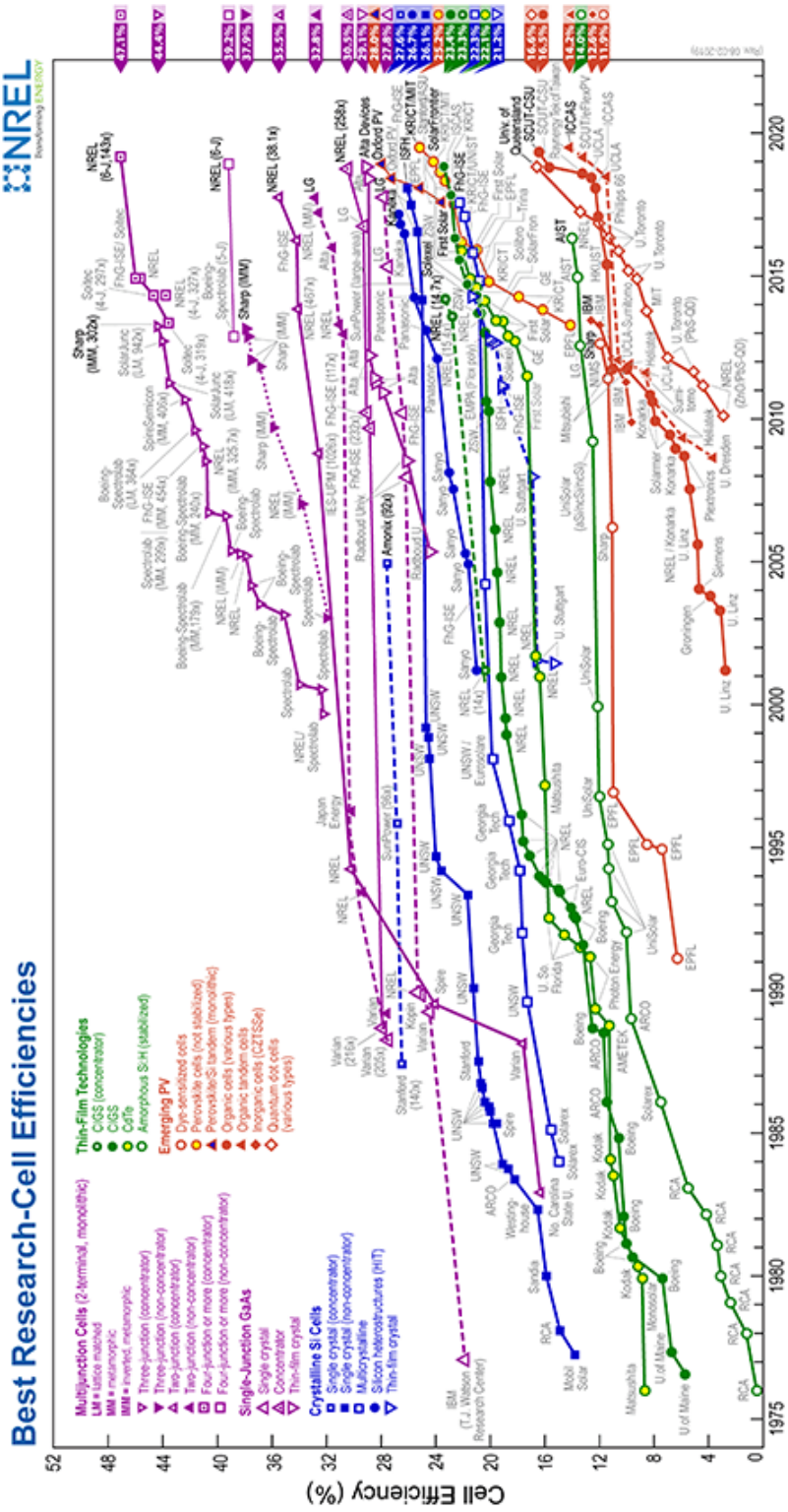

Figure 1.10: Research solar cell efficiency chart, updated to 2019 [15].

Chapter 2

Silicon solar cells

2.1 State of the art

Although other technologies, such as thin-film CdTe or CIGS (see Section 1.3), are experiencing fast developements while becoming more competitive over the market, silicon remains the dominant photovoltaic technology, with more than 90% of the photovoltaic market share [16]. Figure 2.1 shows the growth in market demand of different PV technologies; silicon-based cells account for the majority of annual demand [10].

Silicon has many characteristics that make it a suitable material for the production of solar cells: its bandgap (1.12 eV) is within the optimal efficiency range (see Section 1.2.4), it is the second most abundant element in Earth's crust, is non-toxic and its technology is well mastered by industry [16].
Energy conversion efficiency of laboratory solar cells has reached 25% in 1999 thanks to the PERL (passivated emitter rear locally diffused) cells, and has now reached the record value of 26.63% with the silicon heterojunction technology. The efficiency of wafer-based laboratory modules has reached 24.4% [16].

Theoretically, the conversion efficiency limit of a single junction solar cell has been calculated to be around 30% for 1.1 eV bandgap [13]. Being silicon an indirect gap semiconductor, non-radiative Auger recombination strongly limits the efficiency and sets its limit around 29% [16].

This shows that there is still room for improvement in the efficiency of silicon-based solar cells, even though the limit is close; furthermore, a small improvement in efficiency may have significant impact on the levelized cost of energy (LCOE), the money per unity

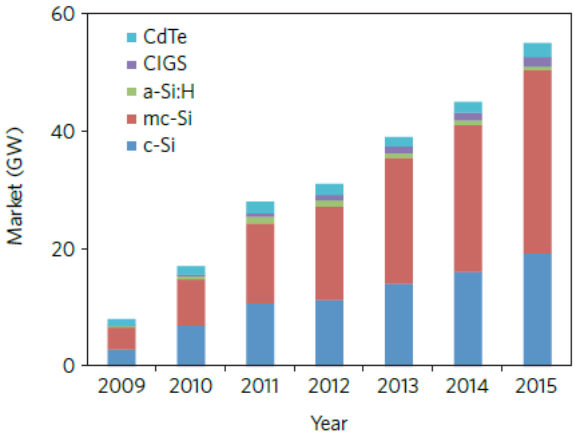

Figure 2.1: Growth in annual PV market demand by technology [10].

electricity that must be made to recoup the lifetime cost of the system [17]. For example, a 10% increase in performance of a commercial module (with efficiency around 17%) can result in a 7.5% decrease in its LCOE [18]. Reduction of the LCOE of PV is key to make this technology competitive with respect to more common energy sources.

2.1.1 Basic structure

The majority of commercial solar cells is based on crystalline silicon. A Si solar cell is a large area diode that efficiently absorbs light at energy higher than 1.12 eV. Silicon cells are made from wafers with a thickness of 0.15 - 0.2 mm and dimensions of 125×125 mm^2 or 156×156 mm^2. Figure 2.2 shows a schematic view of a silicon solar cell.
Some developement of the simple p-n junction structure is needed in order to increase the cell efficiency. It is in fact necessary to mitigate optical and electrical losses and to avoid that light generated electron/hole pairs recombine before reaching the contacts. In the following, some strategies to improve the solar cell efficiency will be presented [19].

- *Surface texturing*, that is, roughening the sunward surface, in order to have more efficient light trapping; the surface of the solar cell is chemically etched in order to obtain a pyramidal structure. This way, light that is reflected upon the first impingement on the cell has a second chance of being absorbed upon the second impingement. Texturing reduces the amount of reflected light of about 11% with respect to a flat surface;

- *Anti-reflection coating* (ARC): a thin layer of a dielectric material, such as TiO_2 or SiN_x is deposited over the surface of the cell. The ARC creates a destruc-

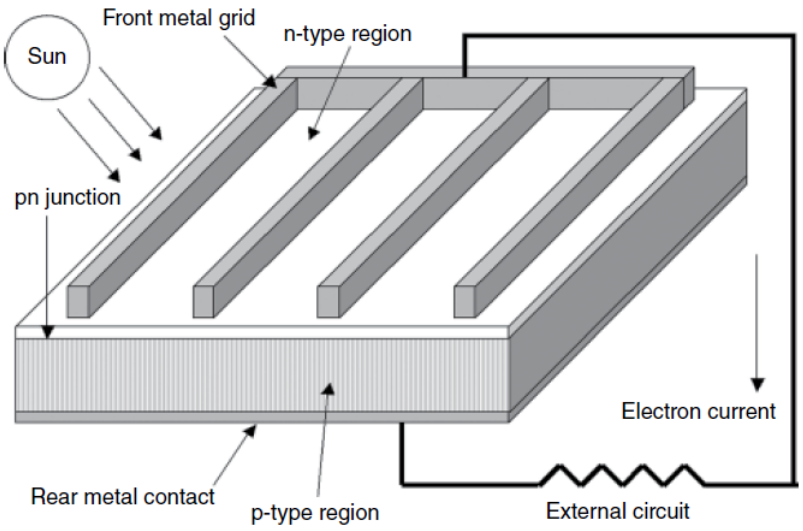

Figure 2.2: Sketch of a Si solar cell with metal contacts [19].

tive interference between the incoming and the reflected light, reducing the latter to a minimum fraction. Anti-reflection coatings have other benefits as well: the dielectric layer provides chemical passivation of surface state, thus mitingating recombination in the device, and it isolates the semiconductor surface from the cell metallization;

- *Front metal contacts*: front contacts cause reflection losses that in turn lower the cell efficiency. Minimizing the dimension and the number of these contacts, that usually have the shape of thin fingers, is necessary;

- *Back metal contact*: the back contact in Si solar cell is usually formed by a metallic (aluminium and silver) sheet that uniformly covers the back of the cell. This ensures that the light that impinges on the back contact is reflected back into the cell. However, back contacts can cause parasitic absorption of a significant fraction of light and also cause the formation of defective states (recombination centres) at the Si/metal interface. Both problems can be solved by the introduction of a thin dielectric layer that prevents parasitic absorption and passivates the surface states;

- *Defect states passivation*: defects in the silicon lattice create states where electron-hole recombination is enhanced. Such defect states are present mostly at surfaces or interfaces. Different materials (commonly, oxides) can be used and deposited as thin films at surfaces/interfaces in order to passivate defect states. Passivating

layers may also be electrically charged, thus creating electric fields that attract one type of carrier and repel the other further reducing the recombination rate.

2.1.2 Screen printed diffused solar cells

The most common solar cells over the past four decades are based on p-type single or multi-crystalline silicon wafers, with screen printing of the metal contacts; the p-n junction is realized by phosphorous diffusion in the front part of the wafer. A sketch of such structure is shown in Figure 2.3. Efficiency of commercial solar cells with this technology is around 15-21% [19].

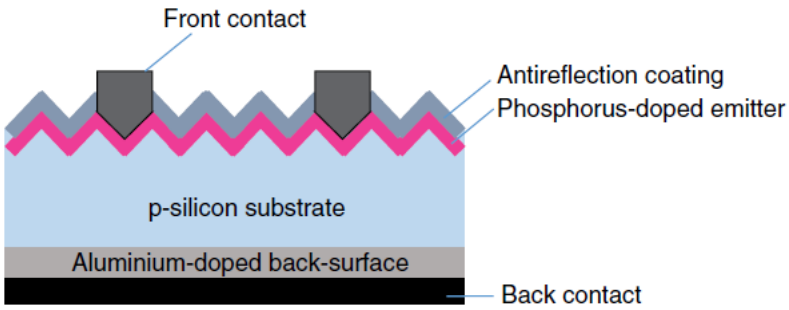

Figure 2.3: Screen printed diffused-homojunction silicon solar cell [19].

Device fabrication

Figure 2.4 shows the basic steps necessary to fabricate a screen printed solar cell. Starting from a p-type crystalline silicon wafer, the first step is texturing, which is done through chemical etching of the silicon surface. Next, phosphorous is diffused through the surface in order to achieve n-doping on the front part of the cell. Deposition of a thin silicon nitride film follows: this has the role of passivating the surface and also works as an anti-reflection layer [19].
Screen printing is used to deposit the metal contacts on the cell: silver paste is deposited in a finger-like structure on the front of the cell, while the back is uniformely covered with a thin film of aluminium and silver paste. In order to bind metal particles together and form a conductive structure, the cell undergoes a step called *firing* (that is, fast -few seconds- thermal annealing). Firing also causes the silver fingers on the front to go through the nitride layer. On the rear surface, the aluminium layer creates the so-called back surface field (BSF): an electrict field forms at the Al/Si interface, repelling minority

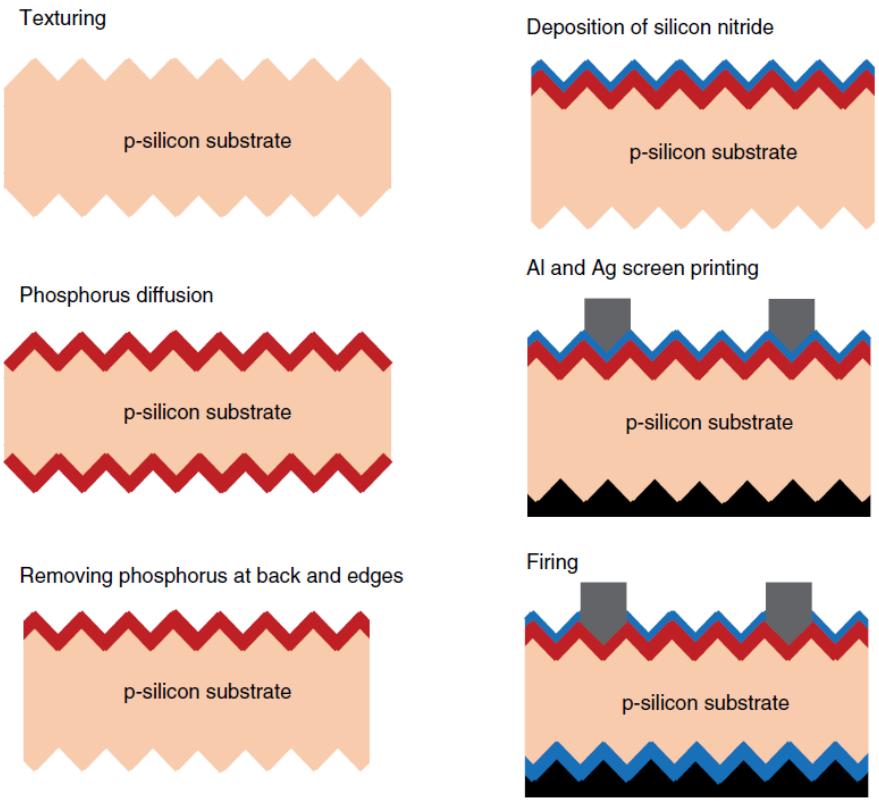

Figure 2.4: Basic steps for the fabrication of a screen printed silicon solar cell with diffused homojunction technology [19].

carriers and reducing recombination [19, 6].
In the end, multiple cells are connected in series to form a module.

Improvements of the screen printed technology

Screen printed solar cells are the dominant commercial technology in the PV sector. In the recent years, innovative cell designs and technologies have been developed; these allow to lower production costs and also improve the efficiency of the solar cells [19].

Selective emitter solar cells: in order to have minimum optical losses, the front contacts of a solar cell should be as narrow and closely spaced as possible. However, this configuration is not optimal in terms of the contact resistance between the metal and the semiconductor, that tends to be quite significant. A way to reduce it is to heavily dope the emitter with phosphorus. While this strategy efficiently reduces the contact resis-

tance, it lowers the efficiency of the cell: phosphorus causes in fact low responsiveness of the cell in the blue and ultra-violet region. The selective emitter technology represents the solution: only the region directly below the contact (3-10% of the surface) is heavily doped, while the other parts of the emitter undergo a lighter doping. The selective emitter configuration is illustrated in Figure 2.5.

PERC and PERL solar cells: Passivated Emitter and Rear Cells address the problem of the relatively high parasitic absorption and recombination rate at the aluminium back contact. A thin layer of a dielectric material is placed between the aluminium sheet and the p-type (boron doped) silicon wafer; this reduces both parastic absorption and electron-hole recombination. An array of small and closely spaced holes is made in the dielectric film in order to establish direct contact between the aluminium sheet and the wafer. Many companies are now introducing PERC technology into production as an upgrade of screen printed cells. A PERC cell is sketched in Figure 2.6.
Passivated Emitter and Rear Local diffusion cells have a structure similar to PERC, with the plus of boron diffusion at the back contact in order to further reduce recombination and resistive losses.

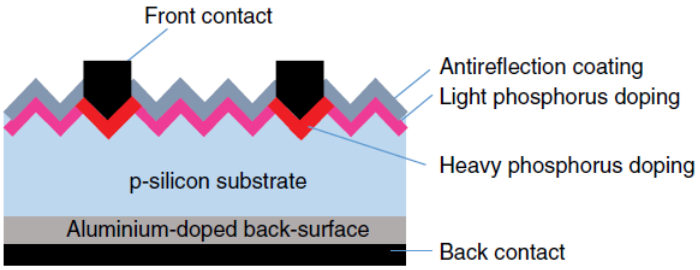

Figure 2.5: Schematic of a selective emitter solar cell [19].

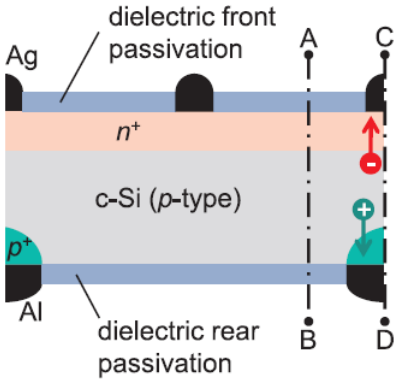

Figure 2.6: Schematic of a PERC solar cell. The front texturing is not shown [3].

2.2 Surface and contact passivation

The surface of crystalline silicon represents an interruption of the periodical structure of the lattice; the presence of this surface creates a high density of defect states in the bandgap that are the cause of carrier recombination. The same problem arises at the wafer/metal interface: the direct contact between a semiconductor and a metal leads to a quasi-continuous defect distribution at the interface, therfore causing high recombination rates in these areas [19].
Since the c-Si wafer quality is steadily increasing, providing longer bulk carrier lifetimes, recombination at the surface or at the wafer/metal interface in a solar cell provides the major fundamental limitation in c-Si solar cells today. Limiting this mechanisms is thus key to improve cell efficiency [3].

2.2.1 Surface passivation mechanisms

Recombination at the surface can be reduced with two different strategies.
The first one is based on the reduction of one type of carrier by the presence of an electric field that repels this carrier type and attracts the other. This electric field can be created by doping the region below the surface. This is the so called *field effect passivation* [19].

The second strategy is based on the reduction of the number of defects at the surface/interface: this can be done by depositing a thin dielectric layer at the c-Si surface, a process known as *chemical passivation*. After the deposition of the thin film, a thermal treatment (e.g an annealing) is required in order to further reduce the defect density by passivating dangling bonds with hydrogen. The most commonly used passivating mate-

rial is silicon nitride (SiN_x); its success is due to the fact that, while it provides a high grade of surface passivation, it can be used at the same time as an anti-reflection coating. Another common material is silicon oxide (SiO_x), that provides the highest passivation quality and allows to reach a conversion efficiency of 25% [19].

2.2.2 Passivating Contacts

Traditionally, the problem of the metal/semiconductor contacts is solved by including a heavily doped region below the metal; in this way, the number of minority carriers and thus the recombination rate is reduced. The metallized area is also kept as small as possible and the highly doped region is confined only below the metallic contacts. Nevertheless, recombination at the metal/semiconductor interface still represents the dominating efficiency limiting factor [19].
It is not possible to apply to metal contacts the same passivation strategy used for free surfaces, since dielectric layers do not allow an efficient charge transport across the contact. The problem can be solved by the developement of the so-called *passivating contacts*, configurations that provide a good surface passivation but at the same time allow to keep the contact resistance very small. These contacts can be used to passivate both metallized and non-metallized areas [3].

Theory

Figure 2.7 shows band-diagrams corresponding to three different situations that allow to understand the requirements that a passivating contact has to satisfy.
In the first diagram (a), the internal voltage is given by the separation of the Fermi energies in the Si absorber ($E_{F,n} - E_{F,p}$). The external voltage is the same as the internal one, $V_{ext} = V_{int}$. This situation corresponds to an ideal case. In the second picture (b), $V_{ext} = V_{int}$ is still valid, but now the internal voltage is limited by recombination losses at the contacts. In the third case, (c), no recombination losses occur, but $V_{ext} \neq V_{int}$: this is due to a voltage drop of the Fermi energy ($E_{F,p}$) that is, majority carriers experience a barrier to transport and are not efficiently extracted at the contact [19].
The ideal case shown in (a) illustrates the two fundamental properties of a passivating contact:

(i) Recombination at the contacts must be suppressed to allow for a high internal voltage: defects at the metal/semiconductor interface must be passivated;

(ii) Any drop in the Fermi energy of the contact region must be avoided so that $V_{ext} = V_{int}$, that is, no barrier to charge transport must be present.

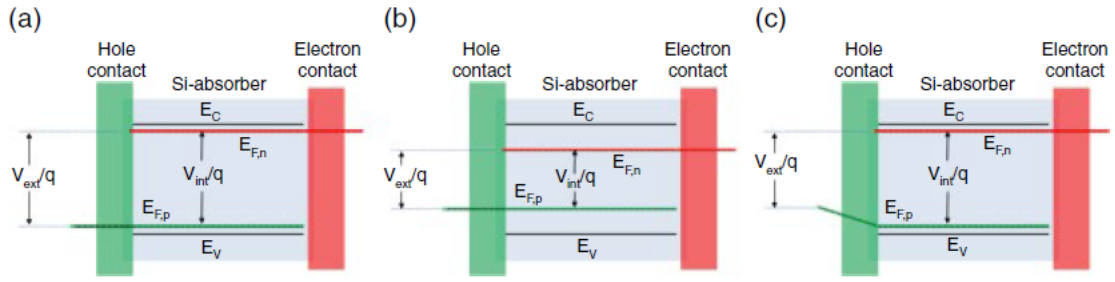

Figure 2.7: Band diagram of a Si solar cells in three different cases: (a) ideal (passivating contact), (b) recombination limited, (c) transport limited [19].

In principle, a passivating contact can be achieved by creating a difference in conductivity between majority and minority carriers: while the former ones are efficiently extracted at the contact (low contact resistance), the latter ones are rejected, thus reducing the recombination rate. Such configuration is known as *carrier-selective contact*. Carrier selectivity is a fundamental requirement for an efficient passivating contact [20].

Experimentally realized passivating contacts

As explained in Section 2.2.1, reduced recombination rates can be obtained both by chemically passivating dangling bonds or by repelling minority carries with an electric field. Passivating contacts commonly use both these approaches [19]. Two main categories of passivating contacts can be individuated:

Heterojunctions: they involve two or more different materials. Carrier selectivity is achieved by depositing films of materials with workfunctions sufficiently different from the Fermi level in the absorber; this induces a potential at the surface, enabling collection of majority carriers and repulsion of minority ones. These films are usually called electron or hole transport layers (ETL or HTL). In case of silicon solar cells, between the contacts and the ETL/HTL, a thin film of a third material is inserted; this acts as a buffer layer and provides chemical surface state passivation. The most successful Si-heterojunction solar cells are based on buffer layers made of intrinsic hydrogenated amorphous silicon for the buffer layers and doped a-Si:H for the carrier selective contacts [2].

Conductor-insulator-semiconductor (CIS): CIS structures have been investigated since the 1970s and were proposed as an alternative to the diffused p-n junction [19].

The conductor can be either a metal (MIS) or a doped semiconductor (SIS) such as highly doped poly-crystalline silicon (poly-Si). A thin oxide is inserted between the conductor and the silicon absorber, providing chemical passivation. Moreover, the heavy doping of the conductor can induce a band banding in the absorber that helps to repel minority carriers and achieves carrier selectivity [2]. A sketch of the basic structure is shown in Figure 2.8.
Since the dielectric has a high bandgap, it creates a barrier to both minority and majority carriers: the main transport mechanism through this kind of structure must therefore be tunneling. This means that the thickness of the dielectric becomes a fundamental parameter that must be controlled carefully: above 1.5 nm, tunneling through the insulator becomes very unlikely [20].
A configuration that has attracted a lot of attention recently is the so-called TOPCon or POLO: poly-Si on an ultrathin silicon oxide. One of the advantages of the TOPCon is that the oxide is stable even for high annealing temperatures, allowing high efficiency but also toleration of existing production processes [4].

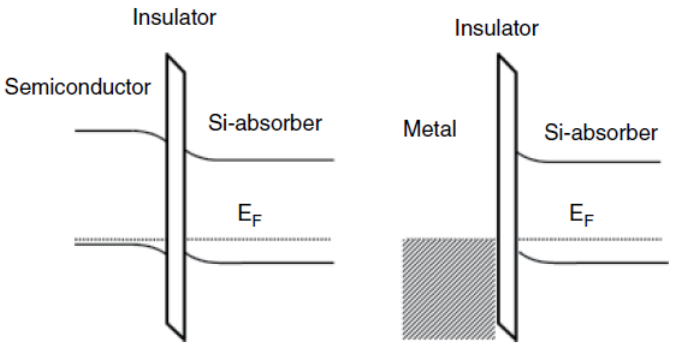

Figure 2.8: Schematic band diagram of a (a) SIS and (b) MIS structure [19].

2.2.3 Fired Passivating Contacts

TOPCon passivating contacts present many advantages that make them a suitable candidate as an upgrade of PERC cells in industrial production. However, the fabrication process of these kind of structures requires a carefully optimized annealing treatment at temperatures around 800°C or 900°C with dwell times up to 15 minutes, which make integration with already existing industral processes more complex. Moreover, TOPCon junctions have so far been applied manly as electron-selective contacts on n-type wafers,

while industrial PV is based on p-type wafers [4].

An alternative approach is the so-called *fired passivated contact* (FPC): a hole-selective contact for p-type silicon cells that can be formed in a single rapid annealing step, a firing, that is currently used in industrial processes for metallization of solar cells (Section 2.1.2) [5].
Figure 2.9 illustrates the structure of a FPC along with its fabrication process.
A thin ($\sim$ 1.2 nm, to allow for tunneling) silicon oxide is deposited on the p-type silicon wafers in order to obtain chemical passivation (2.9 (a)). Later, a layer of a-SiC_x(p):H is deposited on top of the oxide. As firing is a fast (less than 10 seconds, T>750°C, resulting in ramps of 50°C/s) thermal annealing, blistering [1] is an issue for the a-Si layer, that contains hydrogen. In order to solve this problem, the Si-H bonds are strengthened by introducing carbon into the a-Si:H layer, which shifts blistering at higher temperatures. The FPC can thus undergo a firing process (2.9 (c)): the deposited a-SiC_x(p):H partially crystallizes, forming nanocrystalline SiC_x layers. This step is crucial to obtain carrier selectivity: the larger number of active dopants present in the SiC_x layer induces hole accumulation at the c-Si/SiOx interface, which in turn can enhance tunneling through the thin oxide [5].
A sketch of the band diagram of a FPC is shown in Figure 2.10, where a FPC and a traditional poly-Si based contact are compared. In a TOPCon, carrier selectivity is achieved with the presence of a diffused region in the c-Si wafer, that is created during the long annealing process as carriers diffuse from the poly-Si into the wafer. This shallow doped region promotes an efficient band alignment between the wafer and the poly-Si, favouring tunneling thorugh the oxide (Figure 2.10 (c), blue line). In the FPC, the thermal budget of the firing is not sufficient to allow for the diffusion of dopants into the wafer; carrier selectivity is obtained with the hole accumulation region induced by the SiC_x layer [5].
It is thus clear that optimizing the deposition and firing process would allow to obtain controlled properties of the SiC_x layer for an efficient passivating contact, and it is therefore a key step towards an introduction of the FPC technology into the photovoltaic industry.

[1] As a result of the fast ramps, hydrogen bonds can break and effuse from the wafer; if hydrogen effusion is not fast enough, the gas accumulates into the layer and eventually lifts it off the substrate.

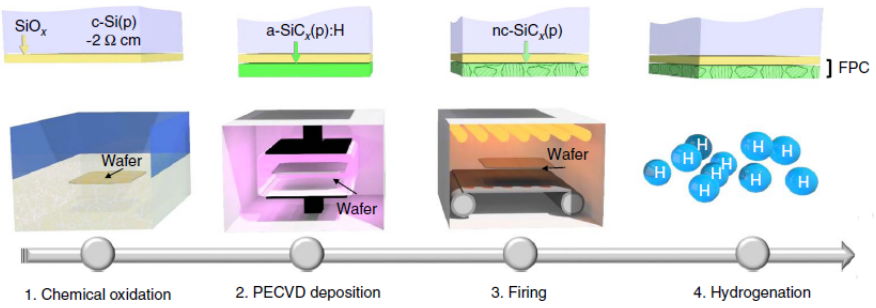

Figure 2.9: FPC fabrication steps: (1) growth of a thin silicon oxide for chemical passivation. (2) deposition of a-SiC$_x$(p):H and (3) firing to crystallize the SiC$_x$ layer. The last step (4) is hydrogenation, that further passivates dangling bonds at the c-Si/SiO$_x$ surface and enhances thermal stability of the structure [5].

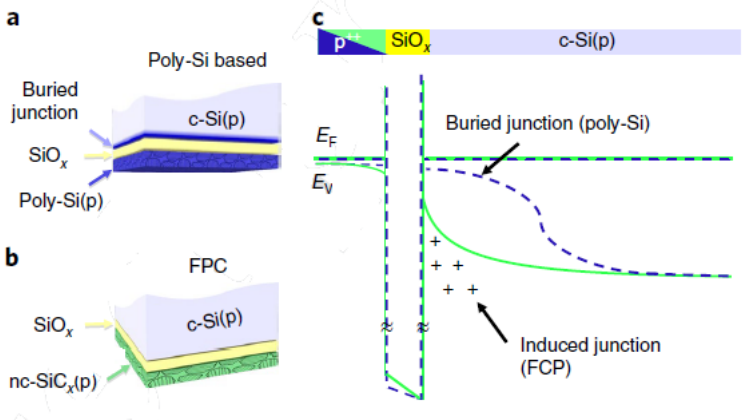

Figure 2.10: Schematic of a (a) traditional poly-Si based PC and (b) a FPC. (c) Comparison bewteen the band diagrams of the two structures: the FPC (green line) presents an hole accumulation region at the c-Si/SiO$_x$ layer, while the TOPCon (blue) shows a buried junction with dopants diffused from the poly-Si [5].

Chapter 3

Experimental methods

In this section, the experimental procedures for preparation and characterization of the samples will be described. The first part is dedicated to the description of the process used for sample fabrication and of the used deposition techniques. The second part of the chapter describes the different characterization methods applied to investigate the electrical and optical properties of the samples.

3.1 Sample fabrication

The samples to measure were prepared starting from float-zone shiny etched silicon wafers, boron doped (p-type). The thickness of the wafers is 200 μm and the sheet resistivity is 2 $\Omega \cdot cm$. After cleaning, deposition of the layers forming the passivating contacts (on both sides of the wafers) was carried out through the following steps (illustrated in Figure 3.1):

- Growth of a thin ($\sim$ 1.2 nm) oxide, either by immersion in a hot (80°C) HNO_3 bath or by ozone under a UV light (Figure 3.1(b));
- Plasma enhanced chemical vapour deposition (PECVD) of a $\sim$30 nm thick SiC_x(p) layer, with excitation frequency of 40.6 MHz at 200°C. The precursors gases were silane (SiH_4), hydrogen (H_2), methane (CH_4) and tri-methyl-boron (TMB, $B(CH_3)_3$) (Figure 3.1(c));
- Firing by rapid thermal processing (RTP) using ramping of 50° C/s, at variable dwell times and temperatures (Figure 3.1(d));
- Hydrogenation to passivate the interface, through PECVD deposition of a thin SiN_x layer and annealing in a firing furnace (Figure 3.1(e));

- Stripping of the nitride layer by immersion in HF (Figure 3.1(f));
- Deposition of ITO/Ag bilayers used as pads for TLM measurements (see Section 3.2.5) by sputtering through a mask (this step was either done after other characterization techniques were used, or only on one half of the samples).

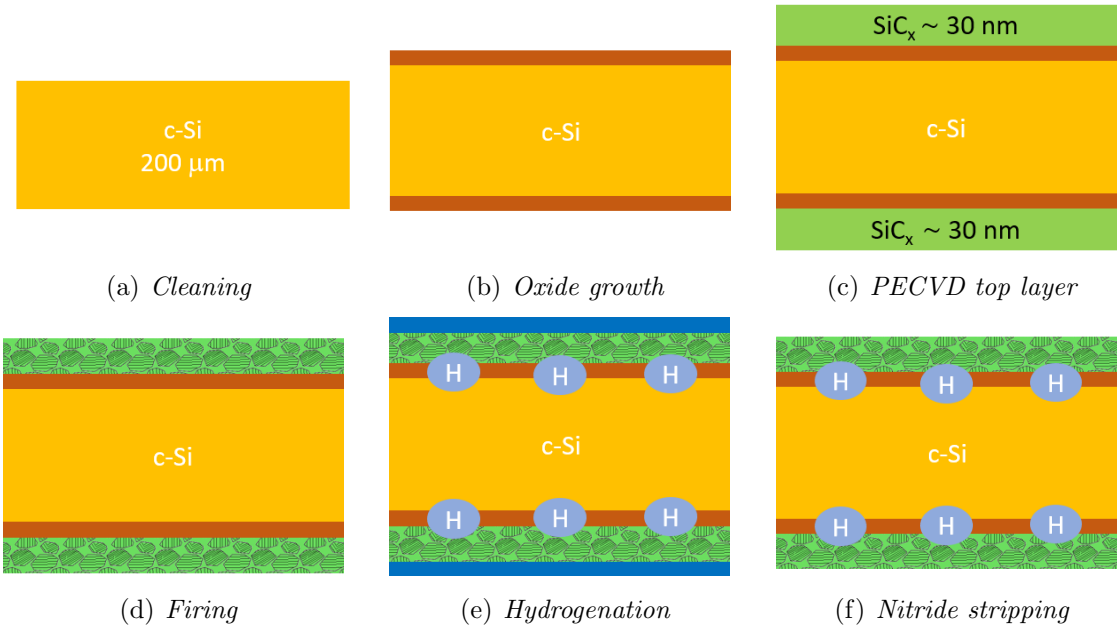

(a) *Cleaning* (b) *Oxide growth* (c) *PECVD top layer*

(d) *Firing* (e) *Hydrogenation* (f) *Nitride stripping*

Figure 3.1: Sample fabrication steps.

3.1.1 Plasma Enhanced Chemical Vapor Deposition

Chemical vapour deposition (CVD) is a widely emplyoed technique for the deposition of thin films on substrates of for high purity bulk material preparation [21]. The deposition process starts with a flow of precursors gases in vapour phase into a deposition chamber, that contains one or more substrates to be coated. A chemical reaction, which can be triggered in different ways depending on the technique that is used, takes place between the precursor gases and the heated substrate. The result of this process is the deposition of a solid film on the substrate.
Thermal CVD relies on heating the substrate in order to trigger chemical reactions with the gases; as an alternative, in the technique known as Plasma enhanced CVD (or PECVD), the gases are ionized through a radio-frequency discharge between two parallel plates. The use of a RF discharge allows to keep the substrate at lower temperatures

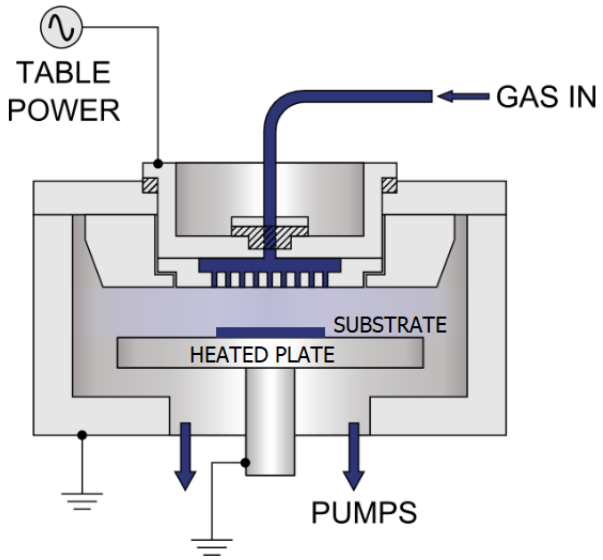

Figure 3.2: Schematic picture of a PECVD system [22].

with respect to thermal CVD, and also results in a fastest growth of the deposited films [21]. A schematic view of a PECVD system is shown in Figure 3.2.

3.2 Characterization techniques

A variety of techniques were used to investigate optical and electrical properties of the samples under study. In the following sections, the different characterization methods are briefly explained, with emphasis on the applications in this thesis.

3.2.1 Surface photovoltage

The surface photovoltage (SPV) method is a well-established contactless technique for semiconductor characterization that relies on analysing illumination-induced changes in the surface voltage. Introduced in the 1970s by Gatos, Lagowski and Balestra, this technique allows to obtain many information about semiconductor bandgap and type, as well as the presence of defect states, in a non-destructive way [23].

The SPV method relies on the analysis of changes in the surface potential of a material under illumination, which represents the SPV signal; it is usually applied in its variant called SPS, surface photovoltage spectroscopy, where SPV signal is monitored as a function of incident photon energy.
The presence of surface or interface states in a semiconductor causes a charge transfer from the bulk to the surface of the material, which leads to the formation of the so called space charge region (SCR); in the SCR, an electric potential is present as a consequence of charge accumulation. This built-in potential leads to a band bending at the material surface. When the semiconductor is illuminated, electron-hole pairs may be generated and separated by the built-in potential. This redistribution of charge leads to changes in band bending with respect to what happens in the dark: the difference between surface potential in the light and in the dark represents the SPV signal that can be detected and analysed. In an SPV spectrum, a change in the slope of the signal can be detected whenever an electronic transition occurs in the semiconductor. This can be a transition from the valence band to the conduction band, whose energy is an indication of the bandgap of the semiconductor, or a transition that involves defect states in the semiconductor.

In Figure 3.3, an example of SPV spectrum for a p-type semiconductor is shown. For energies below E_g, small peaks that are due to the presence of below-bandgap trap states can be observed; for energy that is close to or higher than E_g, transition from VB to CB happens. The red line in the graph represents the ideal scenario, where the signal stays constant above E_g because of a good passivation of the surface, while the grey line shows a decrease in the signal due to surface recombination. This graph shows that the

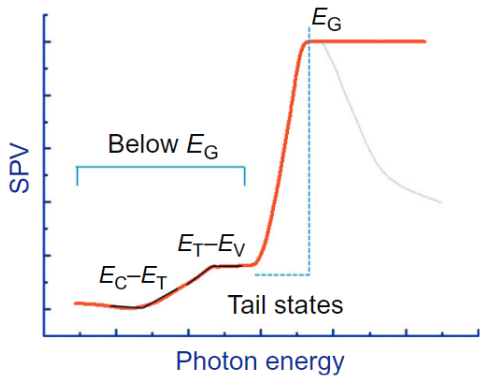

Figure 3.3: SPV spectrum for a p-type semiconductor. The red line represents the SPV signal in the case of low surface recombination, while the grey shows the signal decrease that happens in case of high surface recombination. The peaks labeled with $E_C - E_T$ and $E_T - E_V$ represent transitions between CB/VB and trap states due to defects in the crystal structure [24].

SPV method allows for the measurement of a material's bandgap, as well as detection of defect states and analysis of surface passivation quality [24].

3.2.2 Photoluminescence imaging

Luminescence has been established to be a highly suitable technique for silicon characetization since the work of Peter Wurfel in the 1980s and 1990s, but the real success of this technique was caused by the introduction of luminescence *imaging* methods in the early 2000s [25].
In particular, photoluminesce (PL) imaging finds a wide range of application in the photovoltaics world: this technique exploits optical excitation and therefore it does not require samples to have electrical contacts, as it happens in electroluminescence (EL) [26].
In PL imaging the surface of the sample is excited optically to emit luminescence, while a camera is used to acquire an image of the emission at a fixed wavelength. For applications to silicon, the band-to-band emission with a borad peak around 1140 nm is studied. This analysis is of particular interest for PV applications, since the intensity of the detected signal is linked to physical quantities such as minority carrier lifetime, product of electron and hole densities and Fermi-level splitting [26].

3.2.3 Quasi-steady-state photoconductance

Photoconductance decay is a contactless technique that allows minority carrier density measurement by analysing photoconductance decay transient in a material, after its exposition to a very short light pulse. The minority carrier effective lifetime can be obtained from the slope of the decay curve [27].
A variation of this technique is the quasi-steady state phoconductance method (QSSPC), where a light source is employed, whose intensity varies very slowly with respect to the effective lifetime of the sample under study. This allows to study the photoconductance under different illumination intensities, which can be used to extract useful information like the implied V_{OC} (see Section 1.2.3) from silicon wafers [27].

3.2.4 Raman Spectroscopy

Raman spectroscopy is a spectroscopic technique based on inelastic scattering of a monochromatic light, usually emitted by a laser source. Photons from the source are absorbed by the sample and re-emitted, with a frequency that is shifted with respect to the initial one: this is the Raman effect. The study of this frequency shift can provide information about vibrational, rotational and other low-energy states in solid, liquid or gaseous materials [28].
In the case of silicon, the use of Raman spectroscopy is particularly useful to study the crystallinity of a sample. Crystalline silicon has a charcteristic Raman peak at ~ 520 cm^{-1}, while amorphous silicon shows instead a broad peak around 480 cm^{-1}. In a sample that contains both crystalline and amorphous phases, the crystallinity fraction can be defined as:

$$\chi = \frac{I_C}{I_A + I_C} \tag{3.1}$$

where I_C is the area under the crystalline silicon peak, while I_A is the area under the broad 480 cm^{-1} peak, that can be obtained by a fit from the experimental data [29].
Figure 3.4 shows data relative to two different samples, one amorphous and one that containes some crystal phase, as an example.

3.2.5 Transfer Length Measurements

Transmission line of transfer lenght measurement (TLM) is a technique that allows to easily measure the contact resistance between a semiconductor and a metal contact. It can be shown that the total resistance of a semiconductor with metal contacts at its

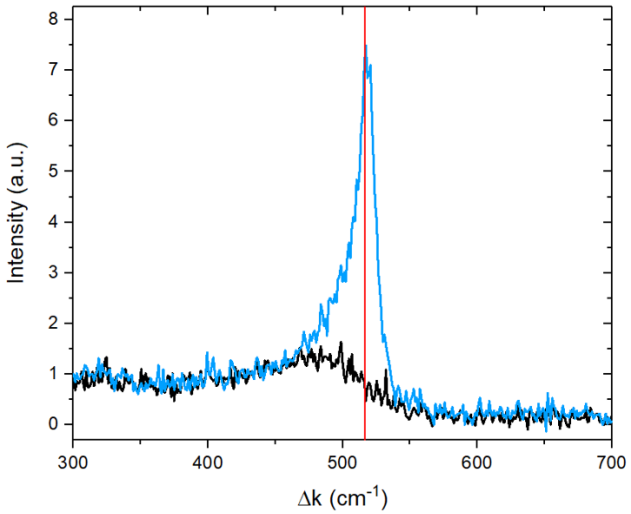

Figure 3.4: Experimental data from Raman measurements of two different samples. The black line is relative to an amorphous sample, that only shows a broad peak around 480 cm^{-1}, while the blue line, with a sharp peak around 520 cm^{-1}, is relative to a sample that is partially crystalline. The red line highlights the peak relative to crystalline silicon.

ends can be written as

$$R_T = R_S \cdot W \cdot L + 2R_C \tag{3.2}$$

Where R_C is the resistance of the metal/semiconductor interface, W and L are the width and length of the semiconductor and R_S is the sheet resistance of the semiconductor [30].

Equation 3.2 shows that, if the length L of the resistor is varied, the intercept of the straight line provides the value of the contact resistance Rc (see Figure 3.5(a)).
A sketch of a typical sample prepared for TLM measurements is shown in Figure 3.5(b), where different metal pads are placed at different distances on the semiconductor.
The quantity that is usually extracted from these measurements is not R_C itself, but the contact resistivity ρ_C:

$$\rho_C = R_C \cdot A \tag{3.3}$$

where A is the area of the contact.

Temperature dependent analysis of contact resistance

The value of the contact resistivity itself can provide useful information about electronic transport in a device, but it can be also useful to study the temperature depen-

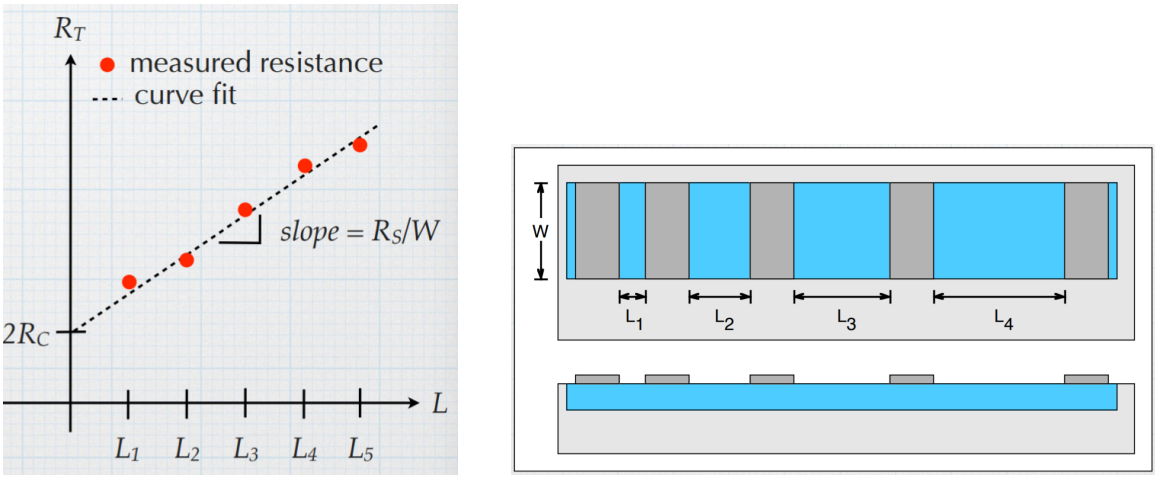

(a) (b)

Figure 3.5: (a) Plot R_T vs L as in Equation 3.2, that shows that the contact resistance R_C can be extracted from a linear fit to data points taken for resistors of different lengths. (b) Top and lateral view of a sample prepared for TLM measurements. The metal pads are placed at gradually increasing distances from one to another, and the blue area represents the part of the semiconductor in which current flows [30].

dence of this quantity. The analysis of the behaviour of ρ_C vs T in a typical oxide tunnel structure (like the Si/SiOx/poly-Si layers sketched in Figure 3.6) allows for example to distinguish between different transport mechanisms in a device, and can be used also to extract quantitative information about material parameters [31].
For the type of samples investigated in this thesis (Section 3.1), a suitable description of the ρ_C vs T behaviour could be given by a combination of tunneling and thermionic emission, described by [31]:

$$\rho_C(T) = \frac{nk_B}{qA^*TP_T} \cdot \exp(\frac{\Delta E_s}{k_bT}) \tag{3.4}$$

where the tunneling probability P_T can be written as

$$P_T = \exp(-d_{ox}\sqrt{E_B\frac{8m_T}{\hbar^2}}) \tag{3.5}$$

and $A*$ is the effective Richardson constant, m_T is the tunneling mass, n the ideality factor and E_B, ΔE_S and d_{ox} are shown in Figure 3.6 [31]. The parameter ΔE_S represents a barrier to transport in these layers, and in principle can be determined from a fit of the experimental data.

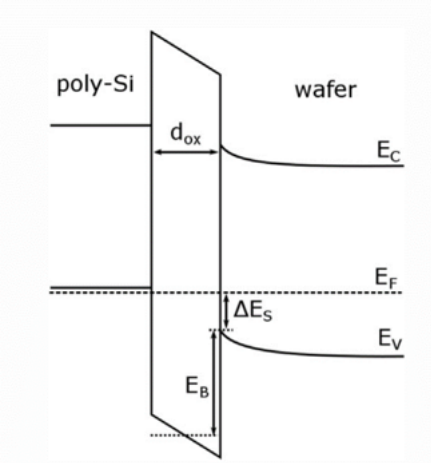

Figure 3.6: Sketch of the band diagram in a Si/SiOx/poly-Si structure. Variations of the parameter ΔE_S change the band-bending at the interface and therefore control transport through the contact [31].

3.2.6 Optical Characterization

Optical characterization was carried out with a combination of three different techniques: Fourier transform infrared spectroscopy (FTIR), spectral ellipsometry and transmission measurements.

FTIR is a popular vibrational spectroscopic technique that employs IR radiation (between 10000 and 100 cm^{-1}) to induce vibrational and rotational excitation of atoms and groups of atoms, that cause absorption of the incident light. In the context of this thesis, FTIR is of interest becuase it allows to study the free carrier absorption (FCA) in a sample, where the photon energy is absorbed by free carriers in the conduction or in the valence band. This kind of absorption is proportional to the carrier concentration of the studied material, and it therefore allows to measure the active carrier density in a crystallized sample [32]. Figure 3.7 shows data points taken from a typical FTIR measurement: the increasing transmission above 0.9 eV is the signature of FCA in silicon.
In the work presented in this thesis shiny etched (SE) silicon wafers were used (see Section 3.1); the surface roughness associated to this type of wafer makes the measurement of FCA more complicated, and so other techniques were used in combination with FTIR to obtain reliable results [33].

Ellipsometry is non-destructive and contactless technique where reflection of light on

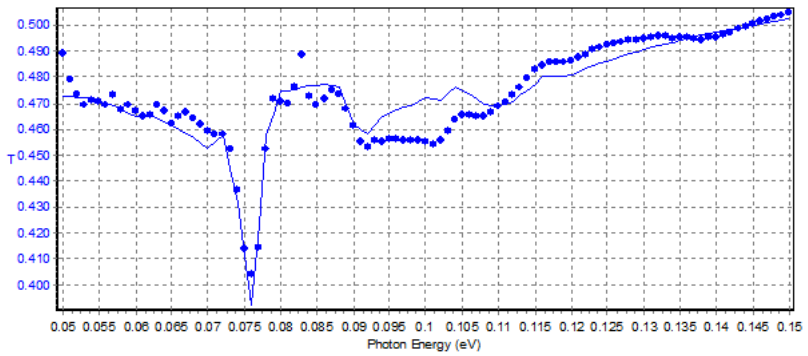

Figure 3.7: FTIR data (dots) and fit (line) for a Si wafer with passivating contacts. The region of interest is between 0.9 and 1.15 eV, where the continuously increasing transmission in the sample is caused by FCA mechanisms.

a sample is studied. In particular, polarized light impinges over a sample at a certain incident angle, and is detected after reflection; interaction with the sample causes the polarization of the light to change. In spectral ellipsometry, polarization changes are monitored as a function of the incident light in a wide spectral range, allowing to exctract information about the optical properties of the sample [34].
In the present work, ellipsometry is used to complete data from FTIR; this is particularly useful for energies above the silicon bandgap (1.1 eV), where primary reflection dominates and the surface roughness of SE wafers does not have a large impact on the measurements. At lower energy, a complementary technique is needed [33].

Total transmission was measured with an integrating sphere around the silicon absorption edge.
The three different measurements were combined in a bound model using a combination of Drude and Tauc-Lorenz models; this allows to fit the experimental data to obtain quantities such as the plasma frequency ω_p and damping constant Γ, from which active carrier density can be calculated [33].

3.2.7 I-V measurements on cells

A few measurements on solar cells containing fired passivating contacts as p-type contacts were done to complete information extracted from the symmetrical samples described in Section 3.1. A sketch of the structure of the studied cells is shown in Figure 3.8.
The measurements perfomed on solar cells are current density-voltage (J-V) measure-

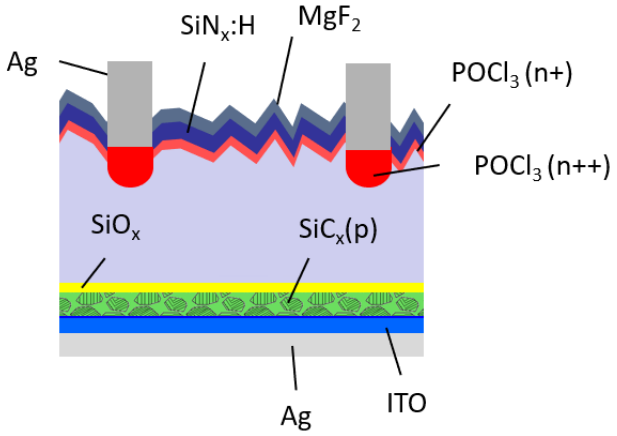

Figure 3.8: Structure of the measured cells. The passivating layers SiO_x/SiC_x are incorporated as hole-selective contacts in the back of the cell, while the front has a selective emitter contact scheme (see Section 2.1.2).

ments in a wide (100-350 K) temperature range: this kind of analysis can provide useful information on the transport mechanism active in the cell. In particular, it is convenient to look at the low temperature behaviour of the Fill Factor (FF - for the definition, see Section 1.2.3), which can be described with the following equation [35]:

$$FF = FF_0^*(1 - r_S) = [\nu_{oc} - ln(\nu oc + 0.72)]/(\nu_{oc} + 1) \cdot (1 - r_S) \tag{3.6}$$

where

$$\nu_{oc} = V_{oc} \cdot \frac{q}{nkT} \tag{3.7}$$

and r_S is the normalized series resistance (see Section 1.2.3 for definitions of paramteres describing solar cells). Sometimes, Equation 3.6 does not describe properly the FF behaviour at low temperature, so an extra term has to be introduced in order to correctly model measured data [35]:

$$FF = FF_0^*[1 - r_{S_1} - r_{S_2} \cdot \exp(\frac{qE_a}{kT})] \tag{3.8}$$

where the new term contains a temperature dependence and the quantity E_a, an activation energy that corresponds to the band bending in the c-Si [35].

An example of the analysis that can be made on the FF behaviour is shown in Figure 3.9, where temperature dependent data relative to two different silicon-based cells featuring two different passivating contacts on the back side are shown. The two different

behaviours of the data sets (black and green lines) can be explained by different transport mechanisms in the passivating contacts. In particular, Equation 3.6 can be used to fit the data represented by the green dots, while the other curve, that shows a FF saturation at low temperature, needs to be modeled using Equation 3.8 [35].

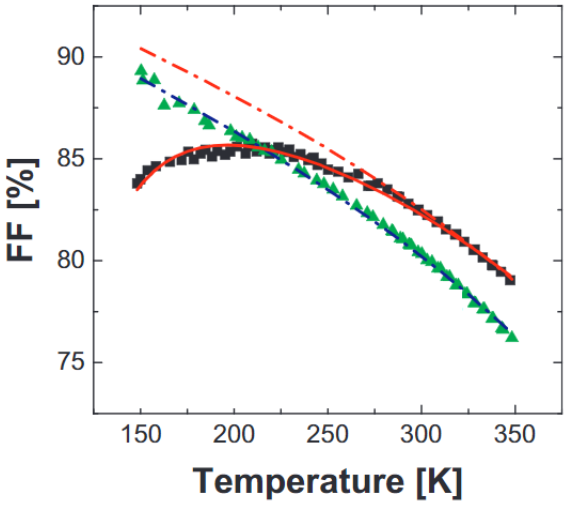

Figure 3.9: FF behaviour for two structurally different solar cells. The dots represent the data points while red and black lines are fits with different equations for the fill factor temperature dependence [35].

Chapter 4

Results and discussion: layer optimization

The first part of the work presented in this thesis was dedicated to understanding how sample preparation conditions - in particular the first firing - influence the electrical and optical properties of the top SiC_x layer in the symmetrical samples (see Section 3.1). The goal of this study was also to find the firing conditions that yield the best properties in the samples.
In this section, experimental results relative to this part of the work will be presented and discussed.

4.1 First measurements on tunnel junction passivating layers: band diagram

The objective of the first measurements carried out on passivating layers was to get a deeper understanding of the band diagram at the c-Si/SiO_x/SiC_x interface, and its relation with sample preparation. To do so, a series of samples with different fabrication conditions was prepared; they are summarized in Figure 4.1 along with results of contact resistance and Raman measurements. This work was done at PV-Lab, EPFL, in January 2019 by researchers in the High Temperature Passivating Contacts group.
A sketch of the sample structure is shown in Figure 4.2.

In the following section, results from contact resistivity vs temperature (PV-Lab, EPFL) and surface photovoltage (University of Bologna) measurements will be presented.

Sample	Oxide	Pre-firing CAMINI	Pre-Firing Jet first	Firing CAMINI	average pc(mΩ·cm2)	Crystallinity
P2 3317	HNO3	770		770	184	no
P2 3316	HNO3	770		800	unmeasurable	no
P2 3315	HNO3	770		830	unmeasurable	no
P2 3327	HNO3	-	770	770	56	no
P2 3328	HNO3	-	770	800	19	no
P2 3329	HNO3	-	770	830	54	no
P2 3330	HNO3		800	770	5.5	yes
P2 3181	HNO3		800	800	too small to be measured	Yes
P2 3304	HNO3		800	830	14.5	Yes
P2 3291	UV-O3		770	770	108	no
P2 3290	UV-O3		770	800	2	no
P2 3303	UV-O3		770	830	unmeasurable	Yes
P2 3294	UV-O3		800	770	5	Yes
P2 3293	UV-O3		800	800	19	Yes
P2 3292	UV-O3		800	830	unmeasurable	yes
P2 3658	UV-O3		830	770	2	yes
P2 3659	UV-O3		830	800	12	Yes
P2 3660	UV-O3		830	830	1.7	Yes
P2 3672	HNO3		830	770	0.7	Yes
P2 3673	HNO3		830	800	0.4	Yes
P2 3674	HNO3		830	830	3.6	Yes

Figure 4.1: Summary of sample properties. The first firing was done either in a furnace at PV-Lab (Jetfirst 200, Jilpelec) or at Meyer Burger, Neuchatel, Switzerland (CAMINI furnace). The column *crystallinity* refers to the presence of the peak at ~ 520 cm^{-1} that can be detected with Raman spectroscopy measurements. *Unmeasurable* in the contact resistivity column refers to the fact that it was impossible to extract a value from the fit, possibly due to problems with the stripping of the nitride layer (see Section 3.1) that caused the I-V curves to be non-linear.

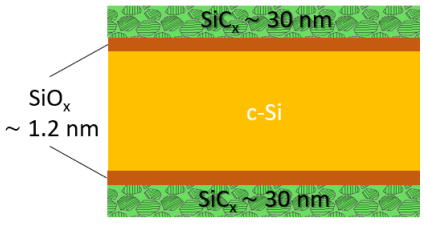

Figure 4.2: Structure of symmetrical samples with c-Si/SiO_x/SiC_x layers.

4.1.1 Temperature dependent TLM

As explained in Section 3.2.5, measurements of the contact resistivity as a function of temperature can provide insight into the band structure of tunnel oxide junctions (an example for p-type layers is shown in Figure 4.3), and individuate the transport mechanisms active in these kind of structures [31]. In particular, analysis of the TLM data allows to obtain values of the surface band bending ΔE_S (see Figure), which may vary depending on how the sample is fabricated and influences transport across the contact.

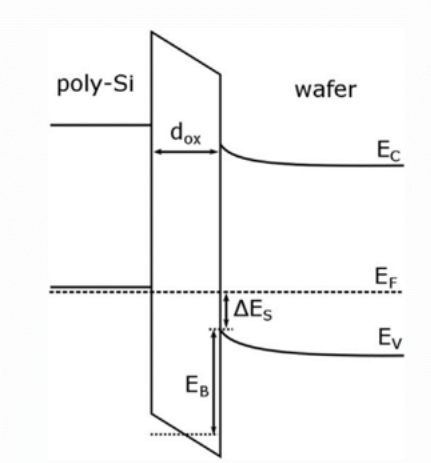

Figure 4.3: Sketch of the band diagram in a poly-Si/SiO_x/Si structure. Variations of the parameter ΔE_S change the band-bending at the interface and therefore control transport through the contact [31].

Procedure

To form the metal contact necessary to the measurement, ITO/Ag pads were deposited on the samples by sputtering using a shadow mask. The mask allowed to obtain three stripes of pads for each sample; they were cleaved along the TLM pattern in order to avoid lateral current spreading. The pads had dimensions of 6× 1.6 mm, and the distance between them varied from 0.25 mm to 5 mm. Since sputtering can also bring to some deposit of material under the shadow mask, real distances between the pads were smaller than theoretical ones; the real distances were measured using an optical microscope. Contact resistivity was extracted from a fit of the data; the values were corrected to take into account current spreading into the samples, according to ref. [36].

Contact resistivity measurements were done in a temperature range between 25 °C and 80 °C using a probe-station with six probes to measure the I-V characteristics of the structure. In order to measure at high temperatures, samples were placed on a hot plate with a T controller.

Results and discussion

Figure 4.4 shows the results from TLM measurements. Only data from some of the samples are shown: in particular, samples with different temperatures of the first firing, but same temperature for the second one were chosen. This choice was made because it was observed that is the first firing that controls layer crystallization and contact resistivty values, while the second one does not have any significant influence on these properties [33].

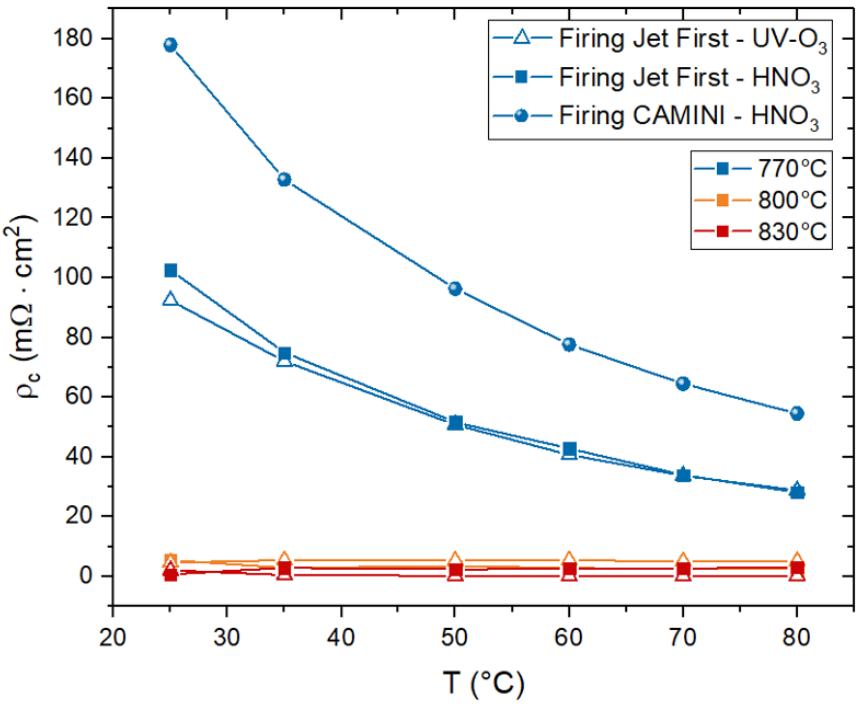

Figure 4.4: Results from contact resistivity vs temperature measurements. Here, only data from some selected samples form Figure 4.1 are shown: the second firing temperature is kept fixed (770 °C), while samples with different temperatures of the first firing are shown.

Data plotted in Figure 4.4 can be divided into two groups: samples with very low ($\sim$ 1-10 m$\Omega\cdot$ cm^2) contact resistivity, that show no temperature dependence, and samples with higher ($\sim$ 100 m$\Omega\cdot$ cm^2 and above) contact resistivity, that seem to have a decreasing behaviour like (see Section 3.2.5 for explanation of the variables and parameters):

$$\rho_C(T) = \frac{nk_B}{qA^*TP_T} \cdot \exp(\frac{\Delta E_s}{k_bT}) \tag{4.1}$$

An Arrhenius plot of $ln(\rho_C \cdot T)$ vs $1/T$ was done in order to fit the data and extract the parameter ΔE_S, corresponding to the difference between the Fermi level and the valence band in the wafer at the c-Si/SiO_x interface. For the high resistivity samples, values of ΔE_S between 180 and 200 meV were found; for the low resistivity samples the data could not be fitted with the proposed model.

At this point, the results were compared with the model for the band diagram of tunnel oxide fired passivating contacts (FPC) proposed in ref. [33]. This model predicts values for ΔE_S that are around 50 - 80 meV, significantly lower than the values found experimentally. A possible explanation would be that the measured value of the barrier ΔE_S is the sum of the two contributions: one from the c-Si/SiO_x/SiC_x tunnel structure, and another one from the Schottky junction between the SiC_x and the ITO used for the TLM pads. This junction creates a barrier to electronic transport, causing the higher value of ΔE_S that was measured. Figure 4.5(a) shows the modeled band structure for tunnel oxide FPC, including also the contribution from the ITO layer.

To decouple the contributions of each barrier on the measured values of ΔE_S, experimental results were compared with the theoretical behaviour of $\rho_C(T)$ for three different cases, shown in Figure 4.5(b): thermionic field emission (TFE, dashed lines) at the Schottky barrier, pure tunneling through the oxide (TO, dotted lines) and a sum of the two (dashed thick lines). The numbers corresponding to the different plots in Figure are relative to different carrier densities measured in the samples [33].
The two groups of samples individuated in Figure 4.4 correspond to the brown and green plots in Figure 4.5(b). Data from a sample which had the first firing at 770 °C, that showed the exponential-like depdendence of contact resistivity on temperature, are represented by the brown dots in Figure; experimental points lie on the line that corresponds to the sum of the tunneling through the oxide and TFE at the Schottky junction.
The green triangles instead correspond to one of the low resistivity samples, that showed no temperature dependence of ρ_C; agreements between data points and modeled behaviour is not perfect, but it can be seen that the measured values lie close to the curve

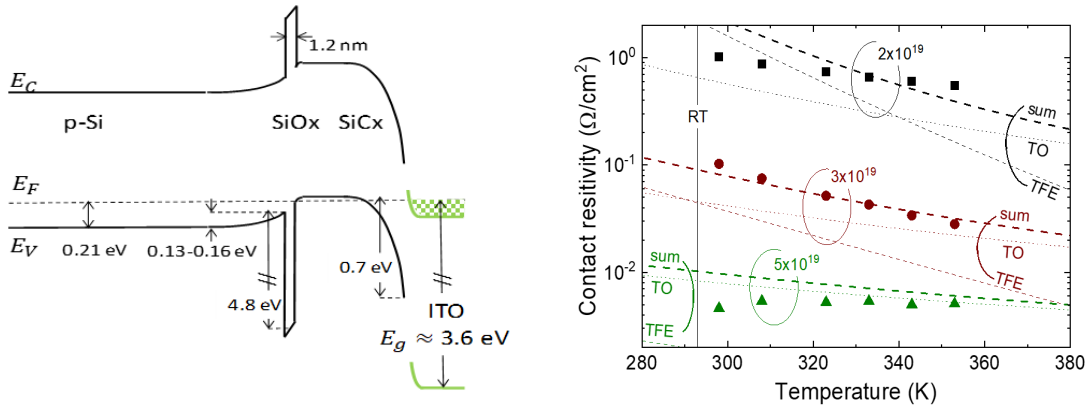

(a) (b)

Figure 4.5: (a) Band diagram for tunnel oxide passivating contacts. (b) Comparison between theoretical and experimental behaviour of contact resistivity with temperature. From [33].

that describes the pure tunneling behaviour. In this case, the barrier at the SiC_x/ITO is not significant, and this yields very low values for the contact resistivity.
Black squares in Figure are data measured from a sample that had very high ($\sim$ 1 $\Omega \cdot cm^2$) resistivity, but this case is not relevant in the context of this thesis, so it will not be discussed any further.

4.1.2 Surface Photovoltage measurements

As explained in Section 3.2.1, surface photovoltage spectroscopy (SPS) measurements allow to detect band-to-band transitions in semiconductors, and are particolarly suitable to study multilayered structures. SPS measurements were therfore carried out at University of Bologna on the samples described in Figure 4.1. The goal of these measurements was to relate changes in the band-bending of the samples to first firing conditions, and provide information about the band structure of tunnel-junction FPC.

Procedure

SPS measurements were carried out using a quartz-tungsten halogen (QTH) lamp as light source, that has a particularly intense emission in the infrared region. This is suitable to study a material like silicon, whose bandgap is around 1.1 eV; moreover, the penetration depth of IR radiation corresponds, in the case of the samples analysed in

this work, to the interface between crystalline silicon and the top layer (SiC_x layer has a thickness of about 30 nm, while the tunneling is oxide is 1.2 nm thick).
Before starting the measurements on the samples, the flux of the QTH lamp was measured using a pyroelectric sensor. Figure 4.6 shows the acquired signal. The acquisition of the lamp flux is necessary for data analysis: the signal measured from the samples was in fact normalized using the lamp flux, through the relation:

$$Normalized\ SPV = \frac{Raw\ signal}{Pyro\ signal} \cdot Energy \tag{4.2}$$

This normalization allows to distinguish between changes in the signal due to samples characteristics and changes that are simply due to the fact that the lamp flux is not flat in a certain spectral region.

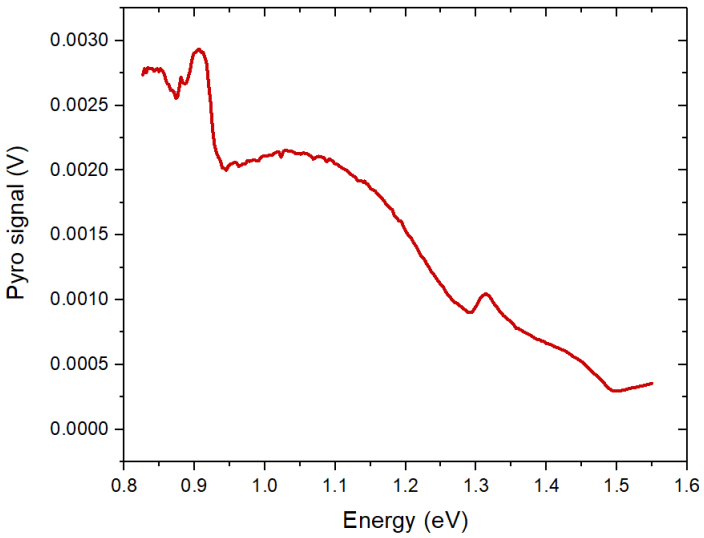

Figure 4.6: Flux of the QTH lamp acquired between 0.8 to 1.6 eV (1500 to 700 nm).

After acquiring the lamp flux, the real measurements were done, using a metal-insulator-semiconductor geometry to acquire the signal [23]. A reference silicon sample without the top SiC_x layers was also measured, in order to compare the data and disitinguish contributions from the silicon wafer from features due to the top layer.

Results and discussion

The first SPV measurements were performed only on some of the samples described in Figure 4.1; samples with varying temperature for the first firing (770 °C or 800 °C), but

fixed for the second one (770 °C) were chosen, like for the TLM measurements described previously (4.1.1). The normalized SPV signal for these samples is shown in Figure 4.7, along with the signal for a reference p-type silicon sample (labeled as 1A).

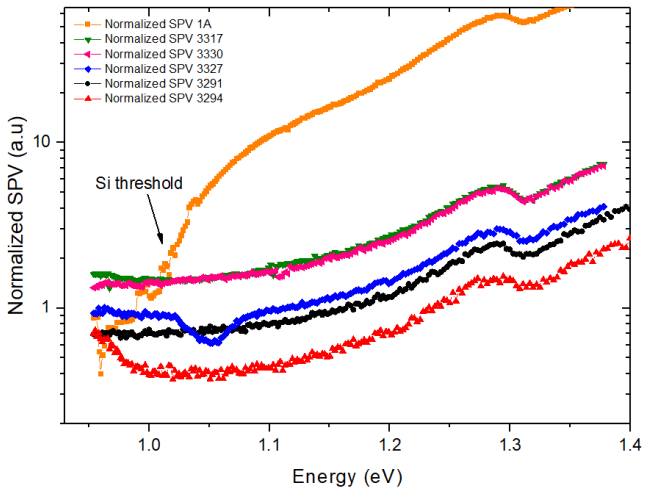

Figure 4.7: SPS data for some selected samples with tunnel-oxide passivating contacts and reference silicon wafer. Data shown are relative to samples that had the first firing either at 700 °C or 800 °C.

Looking at Figure 4.7, no particular feature can be seen in the SPV spectra of the samples. In fact, even the transition relative to the Si bandgap, which is visible for the reference sample (the signal shows a knee around 1-1.05 eV), is absent in the other samples. This could be due to the fact that the tunnel-junction samples are hole-selective contacts, and the signal is thus due to only one type of carrier. The intensity of the signal is therefore lower than for the 1A sample, making the Si bandgap transition less visible. Moreover, since these sample feature some passivating layers, the surface band bending is reduced; the presence of passivting layers reduces the effect of the lattice interruption, which generates charge accumulation at the surface. Since the band bending is reduced, the SPV signal is less intense.

Since no particular feature could be seen in the investigated spectral region, it was decided to perform other measurements at lower energies [37]. This choice was made also according to the results from temperature dependent TLM measurements and the model that was proposed for the bandgap of tunnel-oxide FPC (Section 4.1.1).

Results are shown in Figure 4.8, along with the signal from the reference sample (p-

type crystalline silicon). This time, more samples were investigated; the temperatures reported in the legend are relative to the T of the first firing, while the second firing T can be found in Figure 4.1.

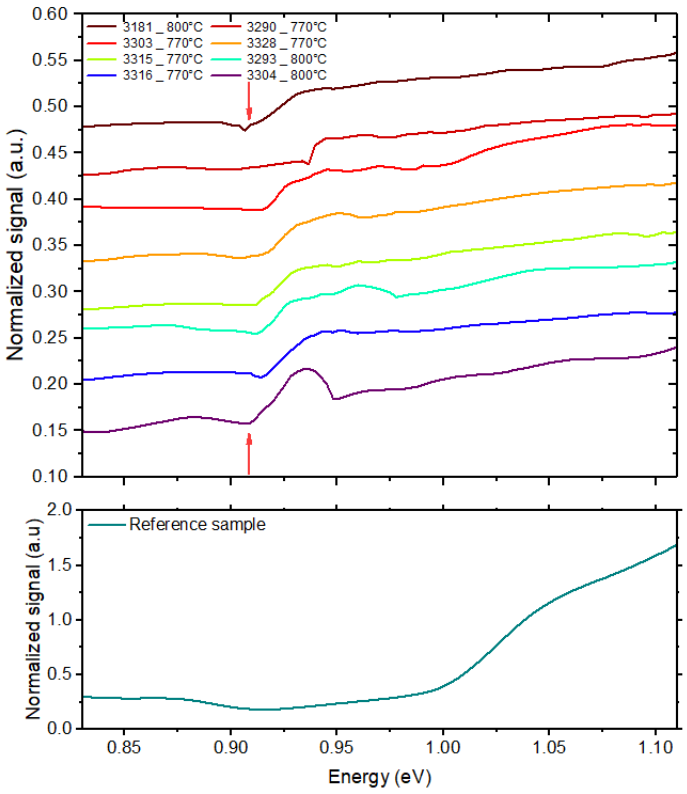

Figure 4.8: SPS data for some selected samples with tunnel-oxide passivating contacts and reference silicon wafer. Data shown are relative to samples that had the first firing either at 700 °C or 800 °C. The investigated spectral region goes from 0.8 to 1.1 eV. A vertical shift was introduced in order to make the plot easier to read. From [37].

In this range, FPC samples show a knee around 0.90-0.92 eV that is not present in the reference sample. Two samples (3304 and 3293) also show a drop of the signal right after the knee. Like it was observed in Figure 4.7, FPC samples do not show any knee that can be related to the Si bandgap transition; instead, the signal increases continuously after the 0.9 eV feature.
In order to explain the knee observed in Figure 4.8, it is necessary to look again at the band diagram proposed for tunnel-junction FPC. Figure 4.9 shows again the diagram, but this time the possible transitions at the c-Si/SiO_x/SiC_x interface have been highlighted. From the values reported in the diagram, it can be seen that the difference between the

SiC_x valence band (VB) and the c-Si conduction band (CB) is around 0.9 eV (transition marked in yellow); the transition between these states could be what causes the knee in the SPV signal observed in Figure 4.8 around 0.90-0.92 eV.

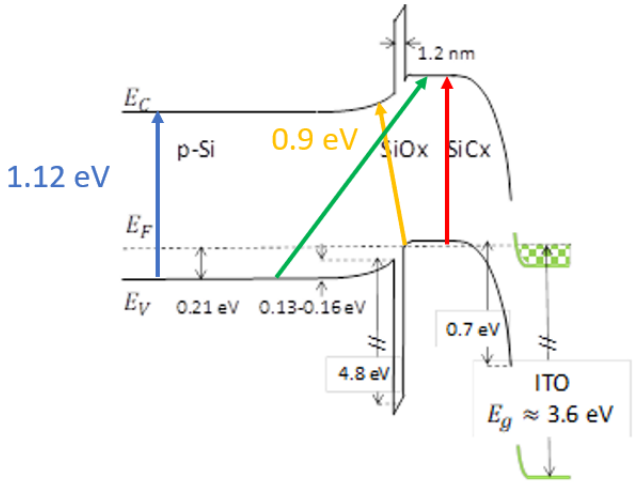

Figure 4.9: Band diagram proposed for tunnel-junction FPC [33]. The possible transitions in the structure have been highlighted.

The transition at ∼0.9 eV could also explain why the silicon bandgap is not visible in the SPV signal shown in Figures 4.7 and 4.8. Carriers that occupy states in the VB of the SiC_x at energy lower than the Fermi energy could also partecipate in the transition; this may cause the continuous increase in the SPV signal that has been observed, that is due to these low energy carriers. This contribution is added to the signal coming from the transition in the c-Si and could mask it, making it unobservable with the SPV method.

It was observed that two samples show an extra feature with respect to the others, a drop of the signal right after the knee at 0.91 eV. It is still unclear how to explain this, but it can be noted that this feature is only present in samples with the first firing made at 800 °C, that were found to be crystalline by the measurements with Raman spectrometer. This feature could then be somehow related to the higher crystallinity of these samples, but further investigation would be needed in order to clarify this point.

4.1.3 Conclusions on SPV and TLM measurements

The preliminary measurements performed on tunnel junction FPC allowed to provide some insight into the band structure and working principles of this kind of devices.

From the study of the contact resistivity as a function of temperature, it was possible to individuate two different transport mechanisms across the passivating contacts: thermionic field emission (TFE), with contributions coming both from the c-Si(p)/SiO_x/SiC_x(p) junction both from the metal contact, is the dominant mechanism for samples fired at 770°C, whereas temperature independent tunneling through the oxide controls transport in SiC_x(p) stacks fired at 800°C. The former is characterized by a strong temperature dependence of ρ_C, while the latter has no contributions from temperature and therfore yields values of ρ_C that are constant over temperature.

Indeed, the tunneling probability of holes through a thin SiO_x (<1.5nm) strongly relies on the alignment of the valence band edges between the SiC_x(p) and the c-Si(p). As the samples fired at 770°C have a lower concentration of electrically active dopants, the supply of holes in the c-Si near the SiO_x and consequently the hole tunneling probability are reduced.
The barrier at SiC_x(p)/ITO is the result of a downward band-bending that is caused by Fermi level pinning or by the work function of the ITO. Assuming Fermi level pinning between the SiC_x(p) and the ITO, as this is typical for metal/semiconductor interfaces, the barrier height does not depend much on the doping concentration within the semiconductor. On the contrary, its barrier width (i.e., depletion width) is doping dependent. In particular, the higher the doping concetration in the Si-doped layer, the narrower the barrier width becomes. The observations presented in the previous section indicate that increasing layer crystallinity and thus amount of electrically active dopants, makes tunneling at both SiO_x and the SiC_x(p)/ITO interface to be the dominant transport mechanism in FPC.

FPC were also studied with the SPV method; some features that change from sample to sample were detected, but it is still not clear how to relate these differences to material properties. A feature around 0.91 eV was detected, that is absent in samples without the top layer: this was explained with a transition from the VB of the SiC_x to the CB of the c-Si. The experimental data agree well with the model proposed for the band diagram for tunnel junction FPC (ref. [33]), that predicts a value of $\sim$ 0.91 eV for this transition. Investigation of the samples in a higher energy range did not show any relevant feature;

the only notable fact is that the transition due to the c-Si bandgap is missing in FPC samples. This could be explained with the lower number of carriers that create the SPV signal in these contacts (only holes are present) or with the presence of the feature at 0.91 eV, that could mask the other transition. Another explaination can be given taking into account the effect of the top layers, whose role is to passivate surface states; this reduces the band bending at the surface, making the SPV signal less intense.

These first measurements provided some information on how sample fabrication affects properties of these layers, but they did not create a complete and clear picture. In the following section, more measurementes made on FPCs in order to further investigate this point will be described.

4.2 Firing conditions optimization

In order to investigate how the conditions of the first firing (from now on, this will be referred to simply as *firing*) influence both the micro-structural properties of the SiC_x layer and the junction quality, a series of symmetrical samples with the same composition of the SiC_x stack was prepared following the procedure explained in Section 3.1, varying only the firing temperature and dwell time. Since the oxide layer can be grown either with HNO_3 or ozone under a UV light, each firing condition was repeated for the two oxide types in order to compare the results. Table 4.1 summarizes the different conditions that were tested.

Firing T (°C)	Dwell time (s)	Oxide type
770	3, 30	HNO_3, UV-O_3
800	3, 30	HNO_3, UV-O_3
830	3, 30	HNO_3, UV-O_3
860	3, 30	HNO_3, UV-O_3
900	3, 30	HNO_3, UV-O_3

Table 4.1: Sample preparation conditions.

4.2.1 Raman spectroscopy

Raman spectroscopy was performed on the samples in order to study the crystallinity of the top SiC_x layer, as explained in Section 3.2.4.

Procedure

Measurements were carried out with a UV laser: since the penetration depth of UV light is very small, this ensures that the collected signal only comes from the top SiC_x layer, without any interference of the underlying crystalline silicon wafer. For each sample, the measurement was repeated in two different points, in order make sure that the sample was uniform. Each measurement was taken by acquiring the signal three different times for 60 seconds each, in order to improve the signal to noise ratio.

Results and discussion

Figure 4.10 shows the results from Raman measurements. Both the series with HNO_3 and UV-O_3 oxides are shown. The acquired signal is shown only in a region of interest around the amorphous and crystalline silicon peaks (see Section 3.2.4), respectively

around 480 and 520 cm^{-1}.
In Figure 4.10(a), both HNO_3 and UV-O_3 oxides can be divided into two sample groups: lower (770-800 °C) and higher (above 800 °C) firing temperature, with the former that shows no peak relative to crystalline material, and the latter that instead has one.
For the series with 30 seconds dwell time (4.10(b)), this difference seems to be less marked, even though it can still be noted that the samples fired at 770 °C have a peak at 520 cm^{-1} that is less intense than for the other samples.

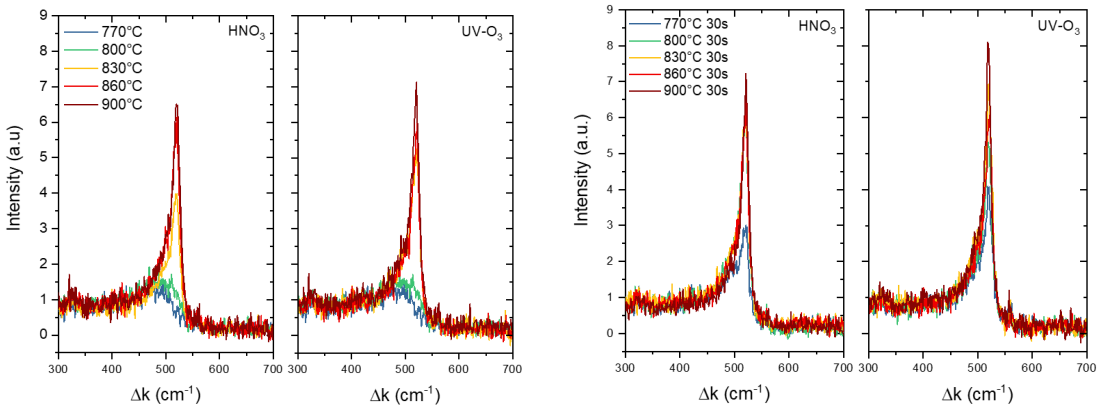

(a) *Series with dwell time 3 seconds.* (b) *Series with dwell time 30 seconds.*

Figure 4.10: Raman results for the two oxides series, showed for different dwell times.

The crystalline fraction was extrapolated from the Raman data as explained in Section 3.2.4. Crystallinity as a function of the firing temperature is shown in Figure 4.11, again for 3 seconds and 30 seconds dwell times.
In both cases, it can be noted that the samples with oxide grown by UV-O_3 show a crystalline fraction that is slightly higher than in the HNO_3 case; this is true especially for the samples fired for 30 seconds (4.11(b)).
Crystallinity shows an increasing trend with firing temperature; it can be also noted that, for a fixed temperature, increasing the dwell time allows to enhance the crystallinity of the SiC_x layer. This effect is particularly evident at lower firing temperatures.

4.2.2 Photoluminescence imaging

PL imaging (Section 3.2.2) was performed on the two (HNO_3 and UV-O_3) series of samples in order to assess the passivation quality of the samples and the uniformity of the top layer deposited by PECVD.

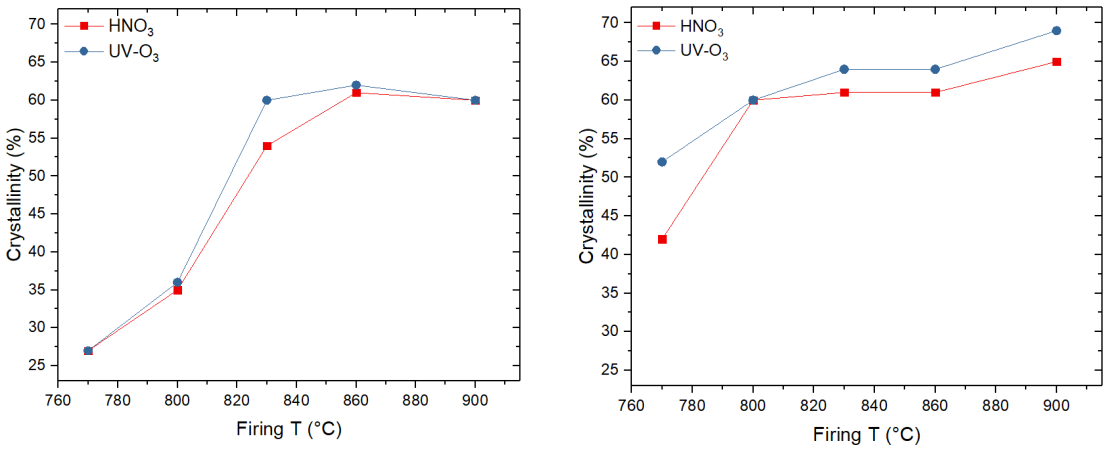

(a) *Series with dwell time 3 seconds.* (b) *Series with dwell time 30 seconds.*

Figure 4.11: Crystalline fraction from Raman data, for the two types of oxides and different firing dwell times.

Procedure

PL imaging was performed exciting the samples with a laser at 808 nm, and detecting the emitted signal with a camera. These samples showed a PL signal that improved with exposure time: a ring shape (signal more intense at the edges) was present in the samples, but this irregularity became less noticeable if the samples were left under the laser beam for a while. Therefore, measurements were taken after exposing the samples to the laser light for 30s, and then acquiring the signal for other 10s.

Results and discussion

Figure 4.12 shows the results only for the samples with oxide grown by UV-O_3, since the two series behaved very similarly.
From observation of Figure 4.12, it is easy to individuate the best firing conditions with respect to passivation of the c-Si/SiO_x/SiC_x interface: the intensity of the signal is linked to minority carrier lifetime, so samples with a very intense PL signal are the ones where recombination of charge carriers is less effective.
For both the 3 seconds and 30 seconds dwell time series, it is evident from the picture that firing temperatures that are too high yield a passivation loss: this can be explained with the fact that samples fired at high temperatures have a high crystalline fraction (see Section 4.2.1), that can be linked to the formation of grain boundaries. These can have detrimental effects on the interface, creating defect states that can act as recombination

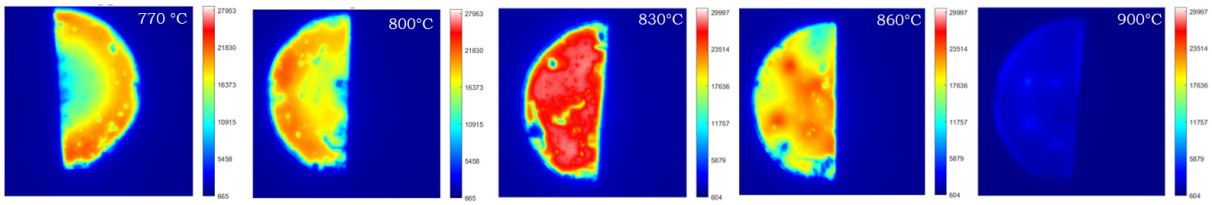

(a) *Series with dwell time 3 seconds.*

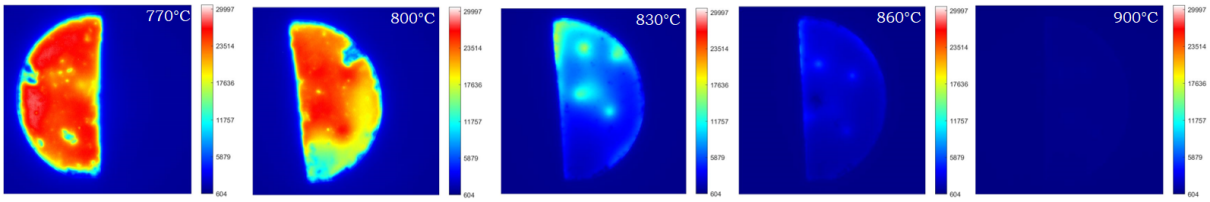

(b) *Series with dwell time 30 seconds.*

Figure 4.12: Series with different firing temperatures as reported in Table 4.1, from 770°C (left) to 900 °C (right), with different dwell times.

centres. For the 3 seconds series, temperatures that are too low (770 °C and 800 °C) create a ring shape in the samples, while the best condition seems to be the firing at 830 °C, that yields a very intense signal. For the 30 seconds series, lower temperatures seem to give better results. Dishomogeneities in the samples, that are visible from PL maps, may have different causes: scratches made during samples preparation, ununiformity of PECVD deposition or of the temperature in the firing furnace.

4.2.3 Transport and passivation quality

In this section, results from QSSPC and TLM (see Sections 3.2.3 and 3.2.5) will be presented together; this will allow to compare the results more easily in order to determine the best conditions for layer preparation.

Procedure

QSSPC measurements were carried out in order to extract the implied V_{OC} for the samples, as explained in Section 3.2.3. This allows to determine how well the interface c-Si/SiO_x/SiC_x is passivated. QSSPC measurements were performed both before and after PL measurements (4.2.2). In fact, the samples showed some light soaking[1] behaviour,

[1]Light soaking effect is described as the ability of a solar cell or PV module to improve its performance after it has been exposed to solar radiation. In the present case, light soaking is used to describe the

and values of the implied V_{OC} became slightly higher after exposing the samples to the laser used for PL. In the following, only values taken after PL measurements are shown.

TLM measurements at room temperature were carried out following the procedure described in Section 4.1.1.

Results and discussion

Figure 4.13 summarizes the results from QSSPC measurements (implied V_{OC}, (a)) and TLM (contact resistivity, (b)). Data for both oxide types and dwell times of 3 and 30 seconds are shown.
Data plotted in Figure 4.13(a) can be compared with the PL maps shown in Section 4.2.2; both techniques detect recombination phenomena at materials' interfaces, and are used to assess passivation quality of multilayered samples. The trend visible in Figure 4.13(a) is very similar to the one shown by the intensity of PL emission in Figure 4.12. For dwell time of 3 seconds, the implied V_{OC} grows with firing temperature, reaches the maximum for $T_{firing} = 830$ °C, and then decreases again, indicating a loss of passivation. For dwell times of 30 seconds, passivation loss begins for $T_{firing} > 800$ °C; the last points in the plot, corresponding to $T_{firing}= 900$ °C, are missing because no signal could be extracted from the sample. This means that passivation is completely lost and the lifetime of minority carriers is unmeasurable. As explained in Section 4.2.2, passivation loss for high firing temperatures could be explained by the high crystallinity of the samples (see Section 4.2.1 about Raman spectroscopy results), that can create some states inside the bandgap; these states can act as recombination centres and explain the decreasing trend of the implied V_{OC} for high T_{firing}. Moreover, from previous tests at PV-Lab it was observed that high temperatures may cause a local disruption of the oxide layer and dopant (carbon or boron) diffusion from the SiC_x into the SiO_x; this phenomenon brings to a degradation of the passivation abilities of the oxide stack.
Implied V_{OC} data shows a difference between the two kinds of oxide: samples with UV-O_3 grown oxide show a higher (~ 10 mV) iV_{OC}, indicating better passivation of the interface.

Figure 4.13(b) shows contact resistivity data; in this case, there is almost no difference between the two series with different oxide types, as the plot of ρ_C vs T_{firing} has the same shape of both cases, and the data points are almost superimposable. In both the 3 and 30 seconds series, samples with higher contact resistance are those that have a lower T_{firing}; as shown in the data from Raman (Section 4.2.1), these samples are the ones

fact that the properties of the material under study improve after prolongued exposition to light [6].

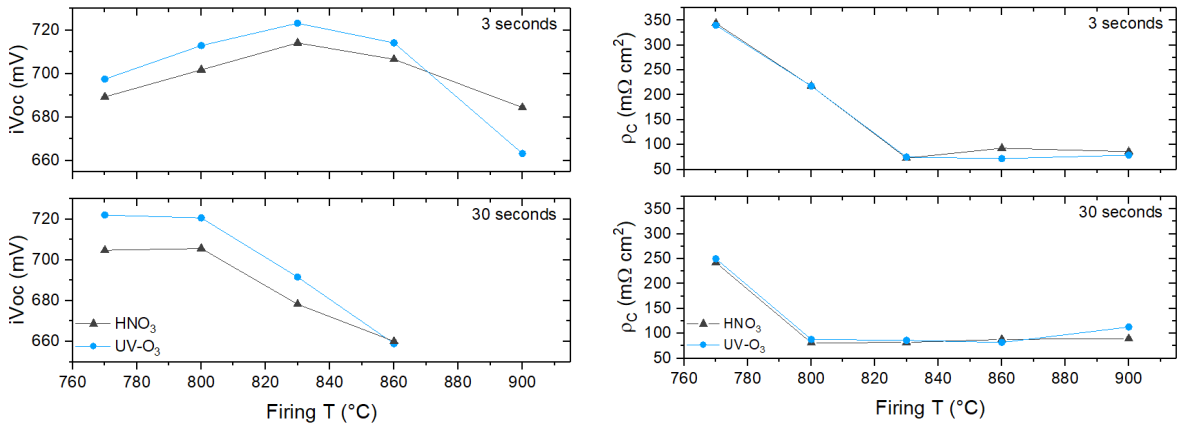

(a) *Implied* V_{OC} (b) *Contact resistivity*

Figure 4.13: Data from QSSPC (a) and TLM (b), shown for both oxide types and dwell times of 3 and 30 seconds.

with a lower crystalline fraction. Electronic transport in amorphous samples is quite inefficient; as the crystallinity of the SiC_x layers grows with firing temperature, contact resistivity becomes lower and reaches a value around 50 $m\Omega \cdot cm^2$ that stays more or less constant for $T_{firing} \geq 830$ °C for 3 seconds dwell time and $T_{firing} \geq 800$ °C for 30 seconds.

By the comparison of the two plots in Figure 4.13, the optimal firing conditions, that yield the best passivation and lowest contact resistivity, can be selected: firing at 830 °C for 3 seconds or at 800 °C for 30 seconds give the best results. In both cases, the oxide grown with UV-O_3 gives higher implied V_{OC} values, and is therefore to be preferred to the HNO_3 oxide.

4.2.4 Temperature dependent TLM

An analysis of the temperature dependence of contact resistivity was carried out on these samples, in the same way as described in Section 4.1.1. Experimental results are shown in Figure 4.14.

The discussion that was already made in Section 4.1.1 holds for these samples as well: two groups can be individuated, samples fired at low (800 °C and below) temperature, where resistivity shows some temperature dependence, and samples fired at high (830 °C and above) T, for which ρ_C has a quite flat behaviour.
Samples of the first group were found to be mostly amorphous from Raman measurements

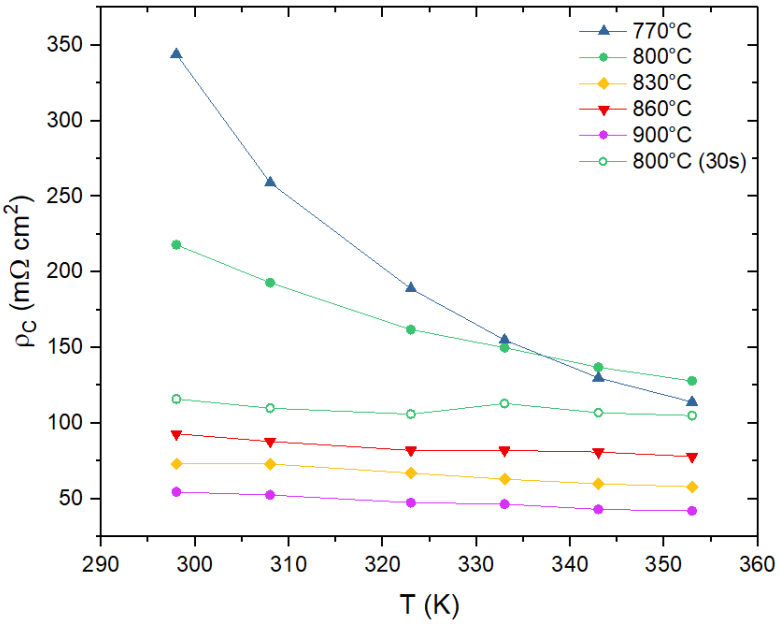

Figure 4.14: Behaviour of contact resistivity vs T, for different firing temperatures. Data for 3 seconds dwell time are shown.

(crystalline fraction below 50%), while the ones in the second group showed partial crystallization of the SiC_x layer. The formation of some crystalline material in the top layer is what causes the transition from a thermionic emission dominated (low T_{firing}) to a tunneling dominated (high T_{firing}) structure, as it is made clear by the comparison of the two samples fired at 800 °C, but for different dwell times (green plots in Figure): 3 seconds are not enough to crystallize the layer, and $\rho_C(T)$ data show some temperature dependence. If the dwell time is made longer (30 seconds), the layer has enough time to partially crystallize even at this temperature, the contact resistivity decreases and the temperature dependence in the data is no longer visible.

4.2.5 Optical measurements

As explained is Section 3.2.6, the study of free carrier absorption (FCA) from FTIR data allows to obtain the active carrier concentration in a sample. In the present case, since the SiC_x layer was deposited on shiny-etched wafers, the surface roughness made the analysis of FCA more complicated; FTIR measurements were then integrated with data from spectral ellipsometry and transmission measurements, as in ref. [33].

Procedure

Transmission measurements in the infrared were carried out using a Vertex 90 FTIR spectrometer from Bruker; the measurements were done over a wide range in the infrared, but the data were analysed only between 0.05 and 0.15 eV. This region was chosen because it allows to study FCA outside the absorption bands of H_2O and other contributions from the environment [33].

Ellipsometry (UVISEL, Horiba Jobin Yvon) was measured between 0.6 and 6 eV, under reflection geometry, with an angle of 70 °.

Transmission was also measured around the Si bandgap, between 0.5 and 1.4 eV using an integrating sphere.

Measured data were then combined into a bound model using both Tauc-Lorenz and Drude model as previously explained.

Results and discussion

Figure 4.15 summarizes the results obtained from optical measurements.
In Figure 4.15(a), the data measured from FTIR are shown in the region around the FCA signature (the increasing transmission above 0.09 eV), measured on samples fired at different temperatures (here, only the data from the 3 seconds dwell time are shown; the behaviour for the 30 seconds series is quite similar). It is evident from the plot that the intensity of the transmitted radiation decreases (or, equivalently, absorption increases), as T_{firing} increases; this effect can be related to a change in the activation of dopants in the SiC_x layer, that was calculated from the plasma frequency ω_p extracted from the fit. Results of this calculation are plotted in Figure 4.15(b).
Data referring to both 3 and 30 seconds firing dwell time are shown. In both cases, an increasing trend is clearly visible, in agreement with what was observed in Figure 4.15(a): increasing T_{firing} favours crystallization in the SiC_x layer and allows to activate a larger fraction of dopants. This fraction in any case remains well below the saturation concentration of boron (the dopant used in this case, see Section 3.1) in silicon; a large fraction of dopants is therefore inactive, possibly because it is incorporated in the amorphous part of the layers [33]. The only exception to this is represented by the point indicated by the red arrow in Figure 4.15(b): the value of carrier density calculated for that sample is so high, that it exceeds the boron solubility limit in silicon for that firing temperature. Further investigation of this point would be needed to explain this result.

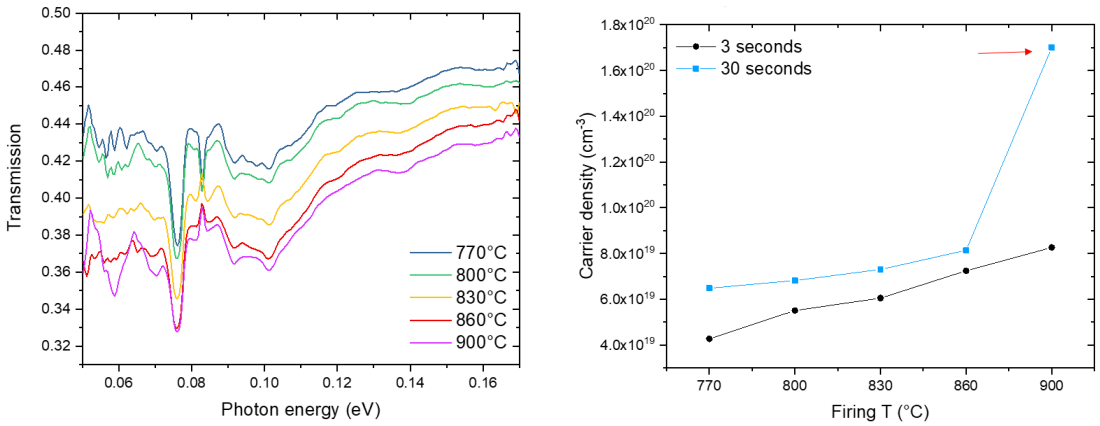

(a) *Free carrier absorption.* (b) *Active dopants concentration.*

Figure 4.15: Crystalline fraction from Raman data, for the two types of oxides and different firing dwell times.

4.2.6 Conclusions on firing conditions optimization

The work presented in this section adresses two main goals:

(i) to further investigate how the firing conditions influence properties of FPC tunnel junction, a subject that was already addressed in Section 4.1;

(ii) to find the optimal conditions to prepare these kind of structures, with particular emphasis on the optimization of the firing, but also comparing the effects that the two different oxide layers (HNO_3 and UV-O_3) have in the structure.

The main results are summarized in the next points.

- It was found that increasing the firing temperature led to the improvement of some properties of the samples: the crystallinity fraction increases as T_{firing} grows, contributing to lower the contact resistivity and to activate a larger fraction of the boron dopants in the layers. The higher the firing temperature, the better these properties are. It was also found that increasing the dwell time contributes to improve these properties of the layers.

- Investigating in more details the transport properties of these layers by T dependent TLM, a threshold firing temperature was individuated: this represents the transition from a thermionic emission dominated behaviour of the samples to a tunneling dominated one. The consequence of this transition is that the samples

no longer show a temperature dependence of the contact resistivity. This threshold firing temperature is also the temperature where the SiC_x layer becomes more crystalline and the room temperature ρ_C exibits a drop (T_{firing} = 830 °C for 3 seconds, and T_{firing} = 800 °C for 30 seconds).

- From the point of view of the passivation, studied by PL imaging and QSSPC, increasing T_{firing} does not always increase the material's performance: in this case, if the temperature is too high and the dwell time too long, a passivation loss is found in the samples. This could be explained by the formation of recombination centres at the c-Si/SiO_x/SiC_x interface, possibly due to the high crystallinity of these layers, and by a partial desruption of the oxide stack due to the high firing temperatures.

- By comparison of the results from samples with HNO_3 and UV-O_3 oxides, significant differences could be noted only in QSSPC measurements, where the UV-O_3 samples exhibited higher implied V_{OC}, and in the Raman, that measured a slightly higher crystallinity for UV-O_3 samples. All of the other measurements that were made did not show any change between the two oxide types.

- Taking into account all the previous points, it was found that the best properties of the SiC_x layer were achieved on samples prepared with UV-O_3 oxide, with either T_{firing}= 830°C for 3 s, or T_{firing}= 800°C for 30 s.

4.3 Importance of the firing

It was explained in the previous sections that firing governs the crystallization of the top SiC_x layer, therefore affecting various other properties of FPC samples. The firing has also another function: to help hydrogen desorption from the sample before the second firing, to prevent blistering that can occour for long (> 10 minutes) annealing time [38].
Previous tests performed at PV-Lab have shown that firing of the SiC layer when capped with a SiN_x, used for hydrogenation, results in layer blistering. As solution, at PV-Lab a two firings step process was developped (see Section 3.1). The first firing is applied to out effuse H from the SiC. Then a SiN_x:H is deposited by PECVD followed by second firing during which H released from the SiN diffuses towards the c-Si/SiO_x interface where it passivates dangling bonds.
Since the goal of investingating FPC is, ultimately, to transfer this technology to industry for the production of cheaper and more efficient solar cells, it is reasonable to try to make the production process as easy as possible. Although in the previous sections it was demonstrated that the two-firing process is capable of achieving high iV_{OC} and low contact resistance it would be convenient to use only one firing to reach both crystallization and hydrogenation of the layers.
In this section, some measurements made in order to understand if it is possible to eliminate the first firing from the fabrication steps will be presented. From now on, the first firing will be indicated simply as "firing" while the second one will be referred to as hydrogenation process.
In order to prevent blistering, the hydrogen quantity inside the sample must be reduced; this can be done by changing the quantities of the precursors gases used in PECVD (Section 3.1) and, more specifically, by reducing the flux of silane (SiH_4).

4.3.1 Sample preparation

An experiment where samples deposited with different silane fluxes were studied was prepared; in this case, the structure of the samples is different from the ones used for experiments described previously, as it is illustrated in Figure 4.16.
The basic structure of the FPC remains (4.16(a)), but the top layer of SiC_x is changed (4.16(b)). In this case, the top layer is formed by three different parts; the central layer is the one where the SiH_4 flux is changed.
A list of the samples and different conditions that were tested can be found in Table 4.2. All the samples were made with oxide grown by HNO_3.

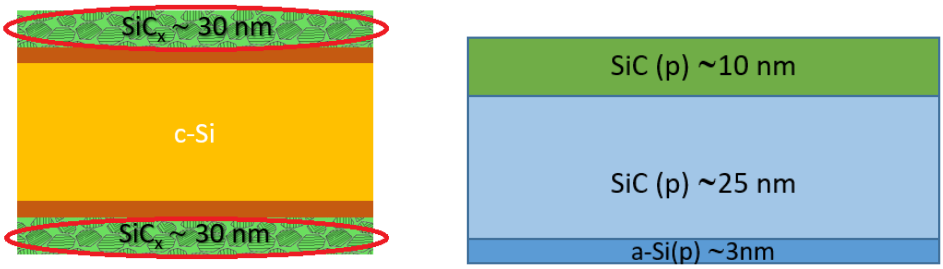

(a) (b)

Figure 4.16: (a) Structure of the symmetrical samples used for this experiment. (b) Close-up on the top SiC_x layer.

Firing (°C)	Silane flux (sccm)
No	95
800	95
No	40
800	40
No	20
800	20

Table 4.2: Sample preparation conditions.

4.3.2 Raman spectroscopy

Raman measurements were performed on the samples in order to determine the crystallinity of the top layer, as previously explained. The procedure that was followed for these measurements is the same as described in Section 4.2.1. Results are shown in Figure 4.17.

It is clear from the Figure that none of the material treatments allowed to reach a high crystalline fraction. Only samples that had a firing treatment show the peak at ~ 520 cm^{-1}, and this is not very intense, corresponding to a crystalline fraction around 40%. For the sample with the lowest SiH_4 flux, crystallization is not reached even with the firing, and the sample remains amorphous.

As the CH_4 flow was not scaled accordingly with the SiH_4 flow, the different layers have a different SiH_4/CH_4 ratio and thus carbon content. The fact that the layers do not

crystallize with SiH_4=20 is due to the large amount of C that prevents layer crystallization.
For samples that were not fired, the top layer stays amorphous regardless of the SiH_4 flux. The sample with highest flux is not shown, because only noise could be measured in this case. This sample, together with the one with 40 sccm of SiH_4, blistered during hydrogenation.

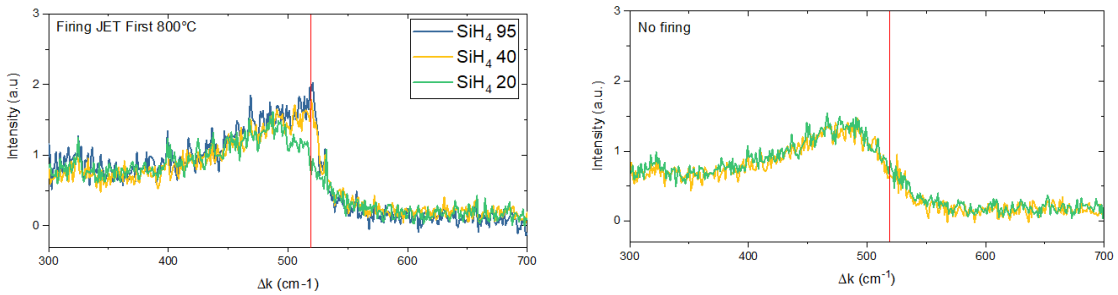

(a) (b)

Figure 4.17: Raman specrtoscopy data for the two firing conditions. The peak relative to crystalline silicon at ∼520 cm^{-1} is highlighted in red.

4.3.3 PL imaging

PL measurements were carried out following the same procedure described in Section 4.2.2. Acquired images are shown in Figure 4.18.
The two samples that were not fired (lower row) and had higher (95 and 40 sccm) SiH_4 fluxes in PECVD deposition blistered during the hydrogenation process, and no data were obtainable from these two samples. This clearly shows that is not possible to eliminate the firing step if the silane flux is not reduced by a significant amount.
The one sample without firing that did not blister has the lowest (20 sccm) silane flux; the PL signal acquired from this sample is nevertheless very low with respect to the samples that were fired (first row). It is interesting to note in this case that, when samples are fired, the decreasing silane flux does not create significant differences in the PL signal. All the samples show a ring shape (like it was observed in Section 4.2.2), indicating some inhomogeneities in PECVD deposition.

4.3.4 QSSPC and TLM measurements

QSSPC and TLM measurements were carried out in order to study the implied Voc and contact resistivity of the samples, following the same procedure illustrated previously

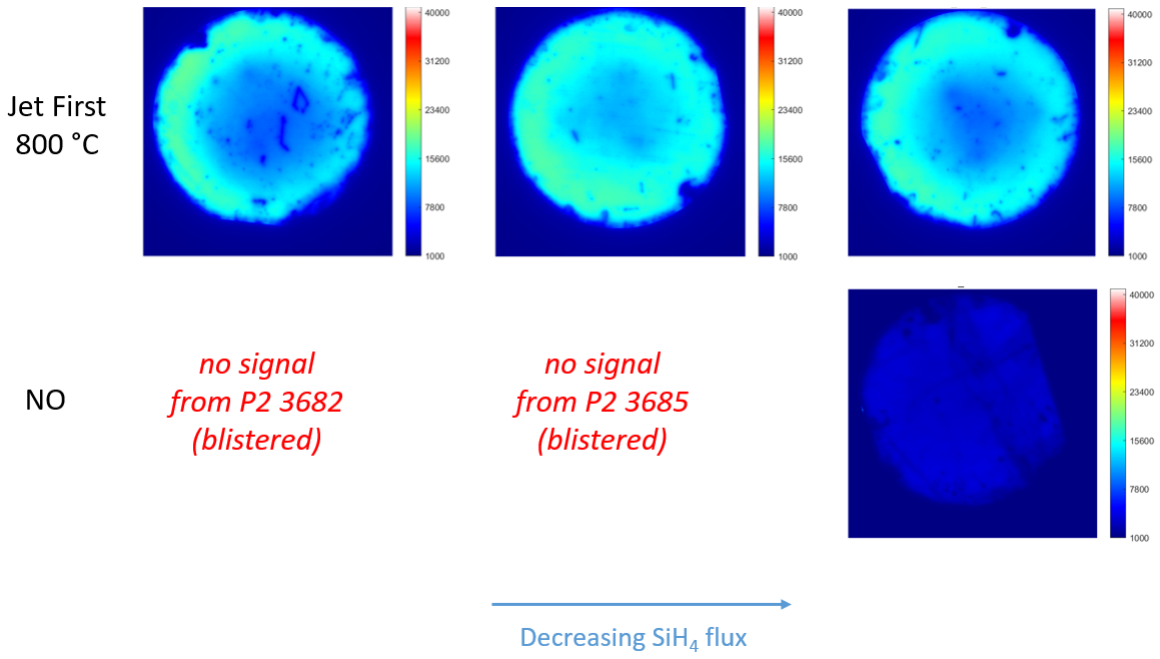

Figure 4.18: PL images acquired for samples with silane flux 95, 40 and 20 sccm (from left to right) and two different firing conditions.

(Sec. 4.2.4). Results are shown in Figure 4.19.
Figure 4.19(a) shows contact resistivity data for samples that were fired. For the other samples, I-V curves were not linear and ρ_C was unmeasurable. The data shown are relative to three different samples for each conditions; maximum, minimum and average ρ_C values are shown. It can be immediately seen that data show a very large dispersion: this could be due to problems with the stripping of the SiN_x layer (see Section 3.1), but also to non uniformities of the PECVD deposition. It is interesting to note that the minimum value measured for the contact resistivity does not change with the SiH_4 flux, remaining constant around a value of 60 $m\Omega \cdot cm^2$.
Figure 4.19(b) shows instead data from QSSPC. Again, the samples that were not fired did not have measurable values for the implied V_{OC}, the only exception being the low-silane sample (in blue in Figure). For the samples that were fired, no particular trend can be individuated in the data. Like previously noted, the changes in the silane flux do not seem to cause significant differences in the different samples.

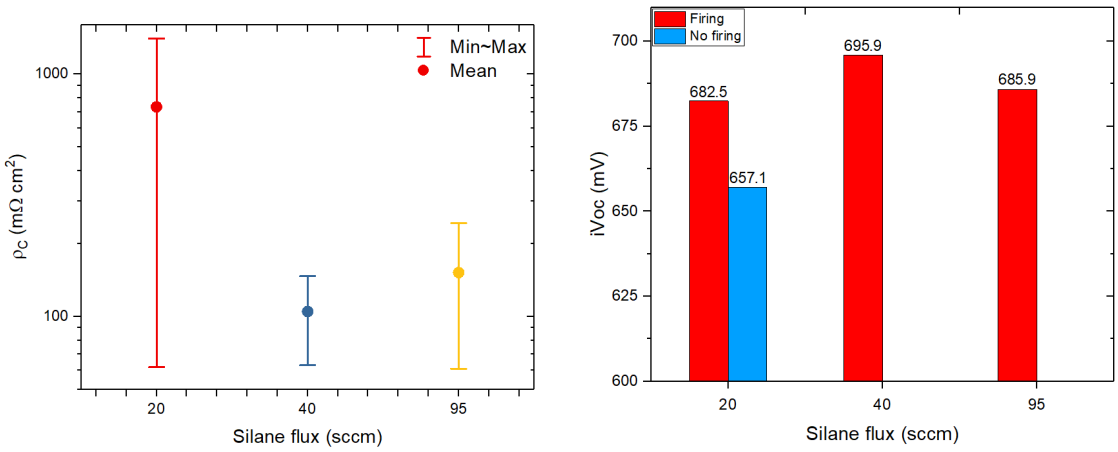

(a) (b)

Figure 4.19: TLM (a) and QSSPC (b) data from measured samples. TLM data in (a) are only relative to fired samples, since no data could be extracted from the other ones. The plot is shown with a logarithmic scale due to the large dispersion of the plotted values. For QSSPC in (b), only one sample without firing showed measurable values for the implied Voc.

4.3.5 Conclusions on silane variations

The goal of the experiment described in this section was to test the possibility of eliminating the firing from the fabrication process, by means of reducing the SiH_4 flux during deposition, and thus the hydrogen content into the samples. It is clear from the results that have just been presented that this is not possible. Comparison between fired and not fired samples clearly show that firing significantly improves the quality of the layer and is essential to prevent blistering.
Only samples with the lowest flux (20 sccm) did not blister during hydrogenation, but these layers did not yield great results. Samples that were fired showed higher crystllinity, better passivation and lower contact resistivity.
Therefore, firing still remains a fundamental process in the fabrication of this kind of layers, and this experiment shows that no valid alternative to it has been individuated yet.

Chapter 5

Results and discussion: the role of passivating contacts in solar cells

In the previous chapter, some properties of FPC have been studied and related one to another through different experimental measurements. All of the analyses were carried out on symmetrical samples; in this chapter, measurements carried out on this kind of samples will be compared to results on actual solar cells. The goal of this study is to understand how different properties in symmetrical samples manifest themselves in solar cells, and how they influence transport mechanisms and operation of the cells. The first part of the chapter will be dedicated to describe the measurements carried out on symmetrical samples. In the second part, solar cells with passivating contacts containing the same layers studied in the first part will be analyzed.

5.1 Symmetrical samples

For the samples studied in this part of the thesis, the basic structure is the same as described previously (Section 3.1, Figure 3.1). In this case, two parameters in sample fabrication were varied: the firing temperature and the flux of TMB (tri-methyl-boron, used for p-type doping, see Section 3.1) during deposition of the SiC_x layer. Table 5.1 summarizes the growth parameters.

The last sample in the table has the top layer made with Si(i)/SiC(p). A thin intrinsic Si layer was introduced to use as a buffer layer in order to prevent degradation of the tunnel oxide due to interaction with carbon or boron diffusing from the SiC during the firing step.

Top layer	TMB flux (sccm)	Firing T (°C)
SiC(p)	20	770, 800, 830
SiC(p)	8	770, 800, 830
Si(i)/SiC(p)	8	770, 800, 830

Table 5.1: Sample preparation conditions.

As the layers studied in this part of the work were processed in a PECVD reactor different from the one used in Chapter 4, they might be slightly different than what was observed previously. For this reason, some measurements and methods already shown in the previous Chapter will be repeated in the current one.

5.1.1 Raman spectroscopy

Raman measurements were performed in order to study the crystallinity of the top layer. The procedure was the same as the one described in Section 4.2.1.
Results are shown in Figure 5.1.

By observing the same sample at different firing temperatures, a confirmation of what was discussed in the previous chapter can be found. Low T_{firing}= 770 °C leads to poor layer crystallization (only the amorphous peak around 480 cm^{-1} is observable). Higher temperatures cause the layer to crystallize more easily and the peak at 520 cm^{-1} appears. These observations are true for all the samples.
The second important observation that can be made is that the highly doped sample (with TMB flux = 20 sccm) shows lower crystallinity with respect to the other two, as it is evident from the peak that is less intense in this case. The crystalline fraction is around 48-50 % in the case of the highly doped sample, while it is above 65% in the case of the other two layers.
This behaviour could be due to the higher density of boron in the top layer; the presence of boron is known to contribute to silane dissociation and thus bring to a faster PECVD growth, resulting in a layer with more disorder and, therefore, lower crystallinity. Additionally, TMB is a gas containing C and C-addition to the Si network is also known for retarding tendency toawrds crystallization. [**?**, 40].

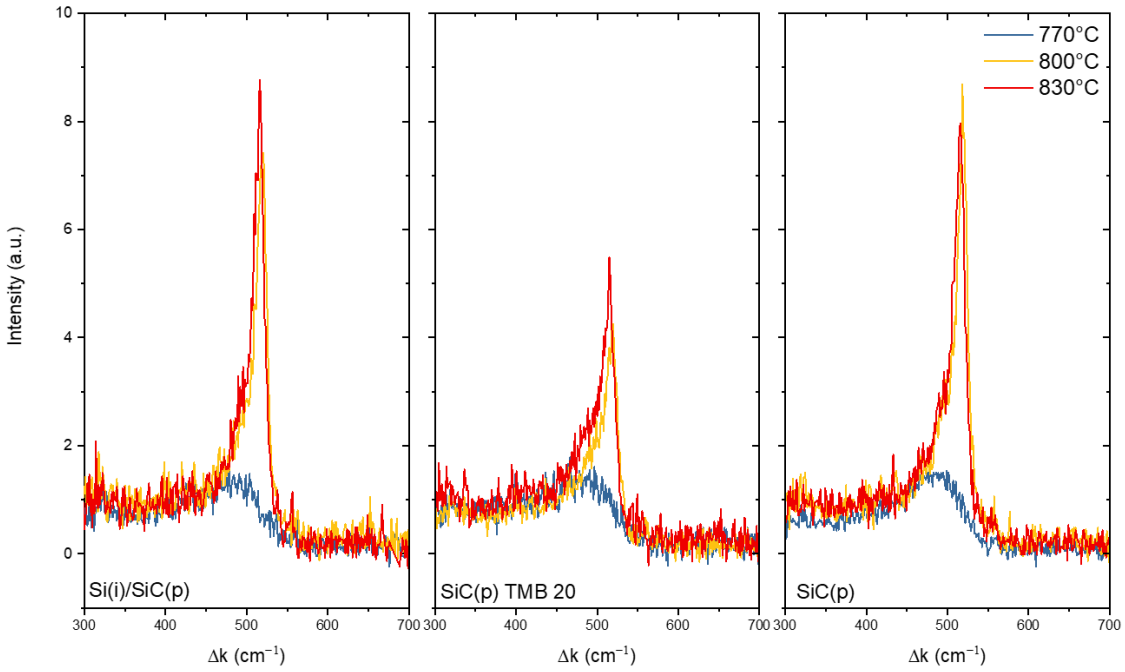

Figure 5.1: Results from Raman spectroscopy measurements. The sample corresponding to each plot is indicated in the lower left corner.

5.1.2 Quality of passivation

As it was explained in the previous chapters, both PL (3.2.2) and QSSPC (3.2.3) can be used to asses the passivation quality of FPCs. Results from these two kind of measurements will thus be presented together. The measurements procedure and the experimental setup have been described in Sections 4.2.2 and 4.2.3.
Figures 5.2 and 5.3 show the results respectively from PL and QSSPC measurements.

Looking at Figure 5.2, it can be seen that all the samples show a high grade of dishomogeneity. This is due to some scratches made during preparation, but also to unhomogeneities in PECVD deposition or firing process.
The PL images acquired for each layer but different firing temperature do not show great differences in terms of intensity; only the images relative to T_{firing}= 770 °C show lower intensity of the signal.
It can be seen that the Si(i)/SiC(p) layer shows less marked differences between a firing T and another; this effect could be due to the presence of the intrinsic Si buffer layer, that allows to make PL emission more homogeneous over different temperatures.

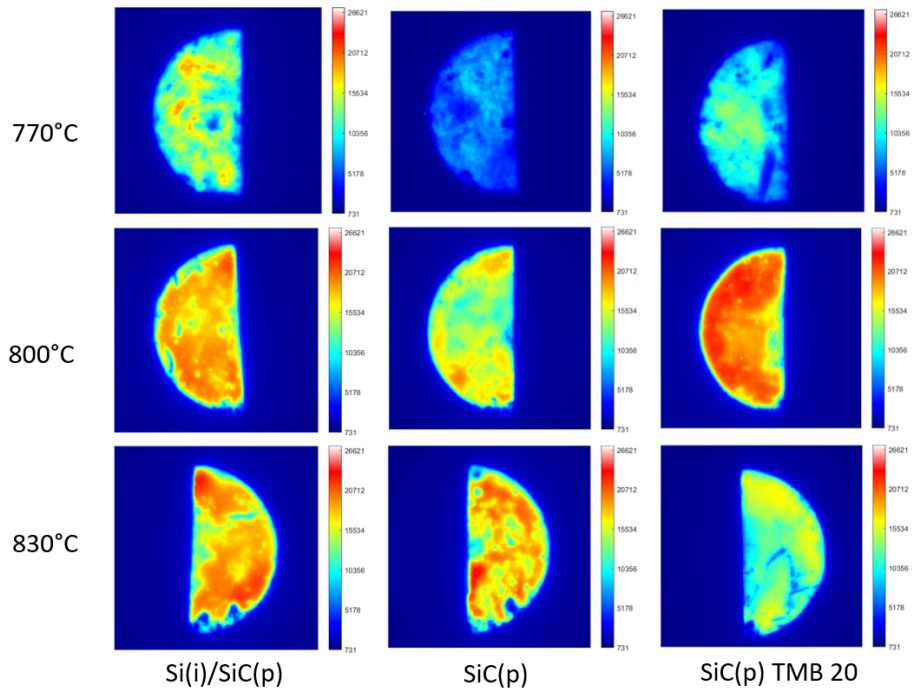

Figure 5.2: PL maps of the samples. Increasing firing T going downwards, layer composition varies from left to right. The intensity scale ranges from 721 counts (dark blue) to 26621 (white).

These observations are confirmed by the QSSPC data, shown in Figure 5.3. No significant differences can be noted between the different layers, while, for each layer, the sample fired at 770 °C has lower implied V_{OC}. The best passivation seems to be brought by the firing at 800 °C, that yields slightly higher iV_{OC}.

5.1.3 Contact resistivity measurements

Contact resistivity of the samples was measured by TLM as described in Section 4.1.1. The data are shown in Figure 5.4. For each layer type/firing temperature, three individual samples were measured. The plot in Figure shows the three individual points and the average value of ρ_C.

The first observation that can be made is that the samples fired at 770 °C show a very high ($\sim$ 1 Ω·cm^2) contact resistivity, that then drops to a value around 100 mΩ· cm^2 for firing at higher temperature. Transport in low-temperature-fired samples is highly inefficient.

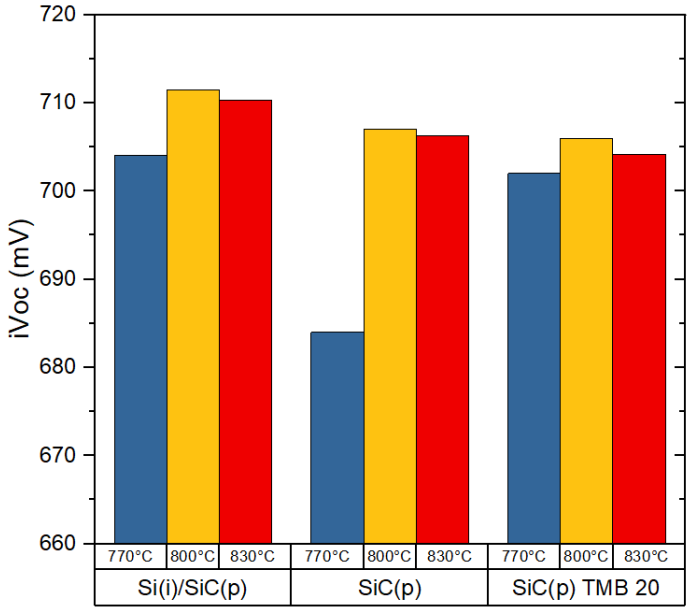

Figure 5.3: Implied V_{OC} data for three different layers at different firing temperature.

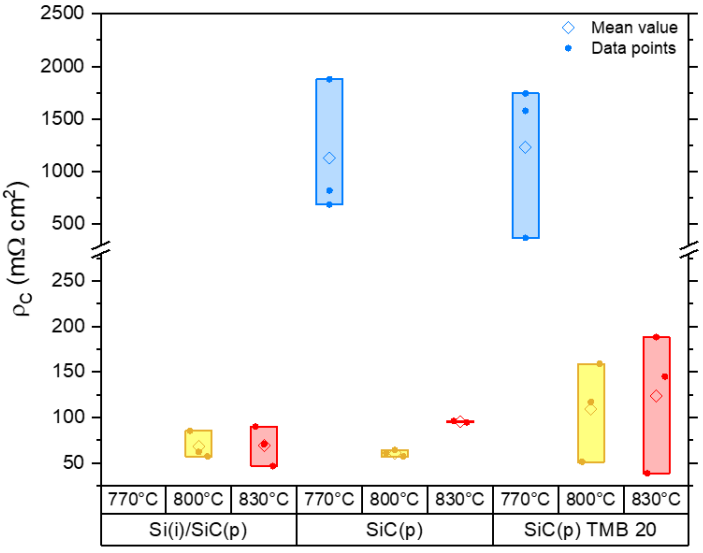

Figure 5.4: Data from TLM. The points relative to Si(i)/SiC(p) layer fired at 770 °C are missing because the contact resistivity was unmeasurable; I-V curves for the sample were not linear and it was not possible to perform the fit.

For higher T_{firing}, data also show a smaller dispersion. The only exception to this are the highly doped layers, that continue to show scattering of the data points even at 800 and 830 °C. This behaviour could be due to the larger amorphous fraction present in these layers, that causes the three individual samples to be quite different one from another. This explaination is also confirmed by the fact that all the (measurable) samples at T_{firing}= 770 °C, that appeared amorphous at the Raman, have the same behaviour.
Another fact to be pointed out is that the average value of contact resistivity for the TMB flux =20 sccm layer is also observed to be higher than for the other cases, both at 800 and 830 °C.
As already observed with QSSPC, the best firing temperature for these layers seems to be 800 °C, which yields the lowest values for contact resistivity.

5.1.4 Temperature dependent TLM

In order to determine if different layers are governed by different transport mechanisms, an analysis of contact resistivity with temperature was carried out, following the procedure described in Section 4.1.1. Figure 5.5 shows the results.
Data from low T (770°C) and high T (800 °C) firing are cleary separable in two groups: the former has samples that show a strong temperature dependence, with ρ_C varying from above 1 $\Omega{\cdot}cm^2$ at room temperature to a value around 400 $m\Omega{\cdot}cm^2$ at 80 °C. The latter has samples that show basically no temperature dependence, with ρ_C values that stay constant below 100 $m\Omega{\cdot}cm^2$.
As discussed in the previous Chapter, these two different behaviours can be related to two different transport mechanisms in the layers: thermionic field emission, with contributions from the tunnel junction and from the ITO of the pads, and pure tunneling through the oxide.
With these measurements, no marked differences between the layers can be noted; the highly doped sample has slightly higher ρ_C when fired at 800 °C, but the temperature dependence is the same as the other two layers.

5.1.5 Optical measurements

FTIR, ellipsometry and transmission measurement were performed on the samples; data were then fitted with a combination of Drude and Tauc-Lorenz models in order to extract the active dopant concentration in the layers. The detailed procedure is explained in section 4.2.5.
Figure 5.6 shows the results of the fit. Data from the SiC(p) layer fired at 770 °C are

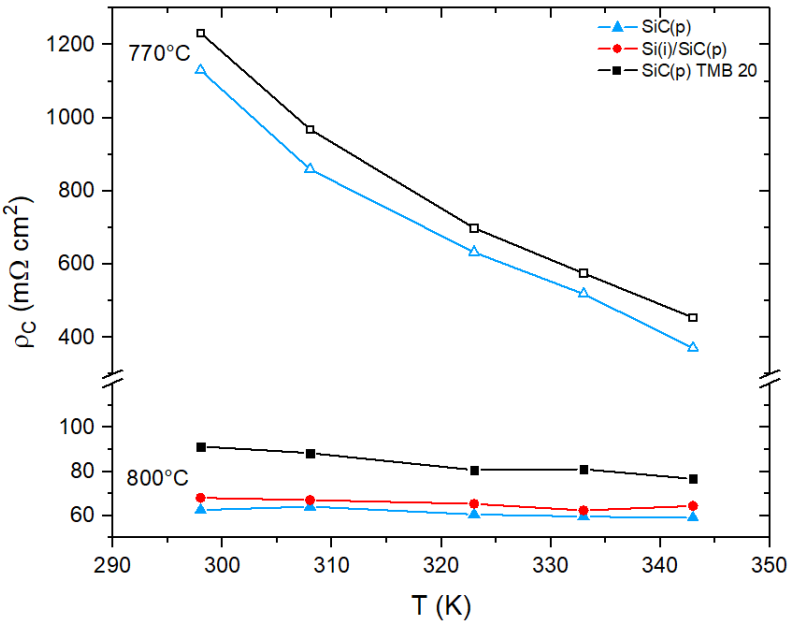

Figure 5.5: Temperature dependent TLM plots. The points relative to Si(i)/SiC(p) layer fired at 770 °C are missing because the contact resistivity was unmeasurable. Data relative to samples fired at 770 and 800 °C are shown; samples fired at 830 °C showed behaviour similar to the ones at 800 °C and are not plotted here.

missing due to problems with the fit, that did not converge.
Two observations can be made about this plot. First, as already observed on different layers in Chapter 4, all layers seem to show a trend of increasing active dopant concentration with increasing firing temperature. This is consistent with the observation that the crystallization of the top layer improves with firing temperature; this is what allows to activate more carriers.
Secondly, the samples with the high TMB flux (20 sccm) show lower carrier density for all firing temperatures. This is again consistent with the data from Raman that showed lower crystallinity for this type of layer. Again, this could be due to the presence of a higher quantitiy of boron, that can contribute to create disorder in the crystal lattice [40, 39].

5.1.6 Conclusions from analyses on symmetrical samples

The measurements on the samples described in Table 5.1 can be summarized by two main conclusions.

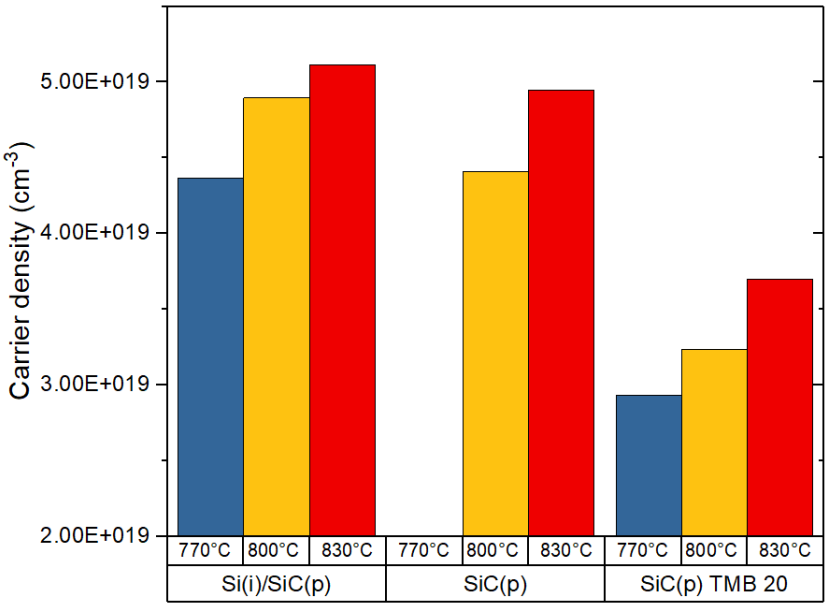

Figure 5.6: Implied V_{OC} data for three different layers at different firing temperature.

(i) The results of these measurements are in good agreement with some results obtained in the previous chapter on layers with different composition and fabricated in different ways. In particular, different properties (crystallinity, active dopant concentration, contact resistivity) of the top layer were observed to show similar trends with changing firing temperature.

(ii) The goal of these measurements was also to compare the different compositions of the studied layers. Concerning several properties, the composition does not play a major role: contact resistivity (both at room temperature and at higher T), implied V_{OC} or intensity of the PL signal showed no trend as a function of the composition of the layers. On the other hand, both data from Raman and optical measurements showed a difference between the two fluxes of TMB used (8 and 20 sccm). Samples that had higher TMB flux, and therefore a higher concentration of boron in the layers, appeared less crystalline and with a reduced concentration of active free carriers.
Even though this difference is visible from optical measurements, it does not seem to influence transport or passivation mechanisms for the conditions under which the measurements were made.

5.2 Solar cells

In the previous section, measurements on symmetrical samples with three different passivating contacts were presented. The goal of this study was to compare the properties measured on test samples with operation of solar cells, to understand how differences in the top layer can influence operational parameters in the cells. To do so, three different cells with the three layers described above were measured.

5.2.1 Sample preparation

The structure of the cells that were studied is sketched in Figure 5.7. The cells were fabricated starting from a p-type cell precursor with $POCl_3$ diffused front contact with SiN_x anti-reflection coating. The p-type contact is a passivating contact with the same structure as already described: interfacial oxide (grown with UV-O_3 treatment) and SiC_x layer (with different compositions). Two firing steps were then applied: the first one (T_{firing}= 800 °C, 3 seconds, Jetfirst) was used to crystallize the layer in the rear side, while the second one (T_{firing}= 830 °C, CAMINI furnace, Meyer Burger) for sintering the Ag paste and hydrogenation of the rear SiC_x.

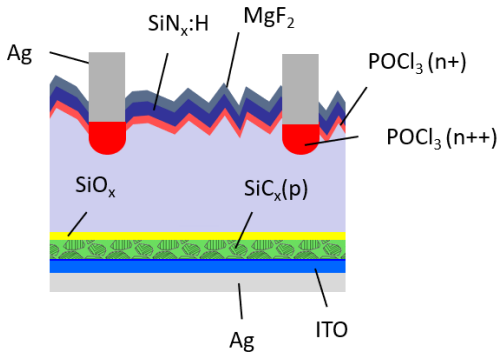

Figure 5.7: Sketch of the measured cell, with $POCl_3$ diffused front contact and p-type passivating contact on the rear side.

Table 5.2 summarizes again the different composition of the three layers (same as in Table 5.1) in the three different cells that were studied.

Top layer	TMB flux (sccm)	Corresponding cell
SiC(p)	20	44
SiC(p)	8	45
Si(i)/SiC(p)	8	47

Table 5.2: Sample preparation conditions.

5.2.2 Temperature dependent J-V

The solar cells in Table 5.2 were studied by means of current density- voltage (J-V) measurements, first at standard test conditions (25 °C, 1 sun) and then in a wide temperature range. These measurements allow better understanding of transport mechanisms in passivating contacts, and understanding of the correlation between some properties of the c-Si/SiO_x/SiC_x tunnel junction with operational parameters of the solar cells.

Effects of temperature on solar cells

Like any other semiconductor devices, solar cells are sensitive to temperature changes, as these modify the electrons' energy in the material and thus the semiconductor bandgap. In a solar cell, the parameter that is most affected by temperature changes is the open-circuit voltage V_{OC} (Section 1.2.3) [6].
The reason for this is the dependence of V_{OC} on the diode saturation current density I_0 (Section 1.2.2). An expression for I_0 can be calculated taking into account only one side of the p-n junction [20]:

$$I_0 = qA\frac{Dn_i^2}{LN_D} \tag{5.1}$$

where q is the charge of the electron, A the area of the junction, D the diffusivity of the minority carriers, L is the minority carrier diffusion length, N_D is the doping concentration and n_i is the intrinsic carrier concentration. Among these quantities, the one that has the strongest temperature dependence is n_i, which behaves as:

$$n_i^2 = BT^3 exp(-\frac{E_{G_0}}{kT}) \tag{5.2}$$

where B is a constant independent from temperature and E_{G_0} is the bandgap linearly extrapolated to absolute zero [6]. From Equation 5.2, it can be seen that n_i^2 decreases with increasing temperature; this behaviour influences I_0 and thus V_{OC}, being:

$$V_{OC} = \frac{kT}{q} ln(\frac{I_{SC}}{I_0}) \tag{5.3}$$

From Equation 5.3 it is possible to extract the temperature dependence of V_{OC}, which decreases with increasing temperature. Moreover, the dependence of the short-circuit current can be obtained as well; I_{SC} increases slightly with temperature [6].

Procedure

J-V measurements were carried out on the solar cells at standard test conditions first, and then by changing temperature.
The samples were placed on a heatable chuck, connected to a temperature controller. The system was cooled down to $\sim$ 150 K using liquid nitrogen; after waiting for the temperature to stabilize, the temperature control was turned on and the chuck was heated gradually by exploiting the peltier effect. A measurement was taken every 5 degrees under different illumination conditions. Data were measured between 150 and 350 K.
The acquisition program allowed to directly calculate operational parameters of the cells (V_{OC}, J_{SC}, efficiency and FF, see Section 1.2.3) during data acquisition.
The behaviour of these parameters with temperature was then analyzed, as explained in Section 3.2.7.

Results and discussion

Table 5.3 summarizes the main parameters used to describe solar cells, obtained by J-V measurements at standard test conditions. The values for the different parameters are slightly different from cell to cell, but overall there are no significant differences visible from these measurements.

Cell	Efficiency (%)	J_{SC} (mA/cm^2)	V_{OC} (mV)	Fill Factor (%)
44	21.94	41.1	679.8	78.52
45	22.08	41.5	680	78.23
47	22.34	41.6	679.7	79

Table 5.3: Results from J-V measurements at 25 °C, 1 sun illumination.

Figure 5.8 shows temperature resolved data acquired from the three cells; short-circuit current density J_{SC}, open-circuit voltage V_{OC} and fill factor are shown respectively. By looking at Figure 5.8 (a) and (b), there are no significant differences in the shape of the J_{SC} vs T or V_{OC} vs T curve. For the open-circuit voltage, data are almost perfectly superimposable. Current data show a drop at low temperature for cell 45, probably due

to a bad contact with the probes, but the shape of the curve is the same for all of the three cells.

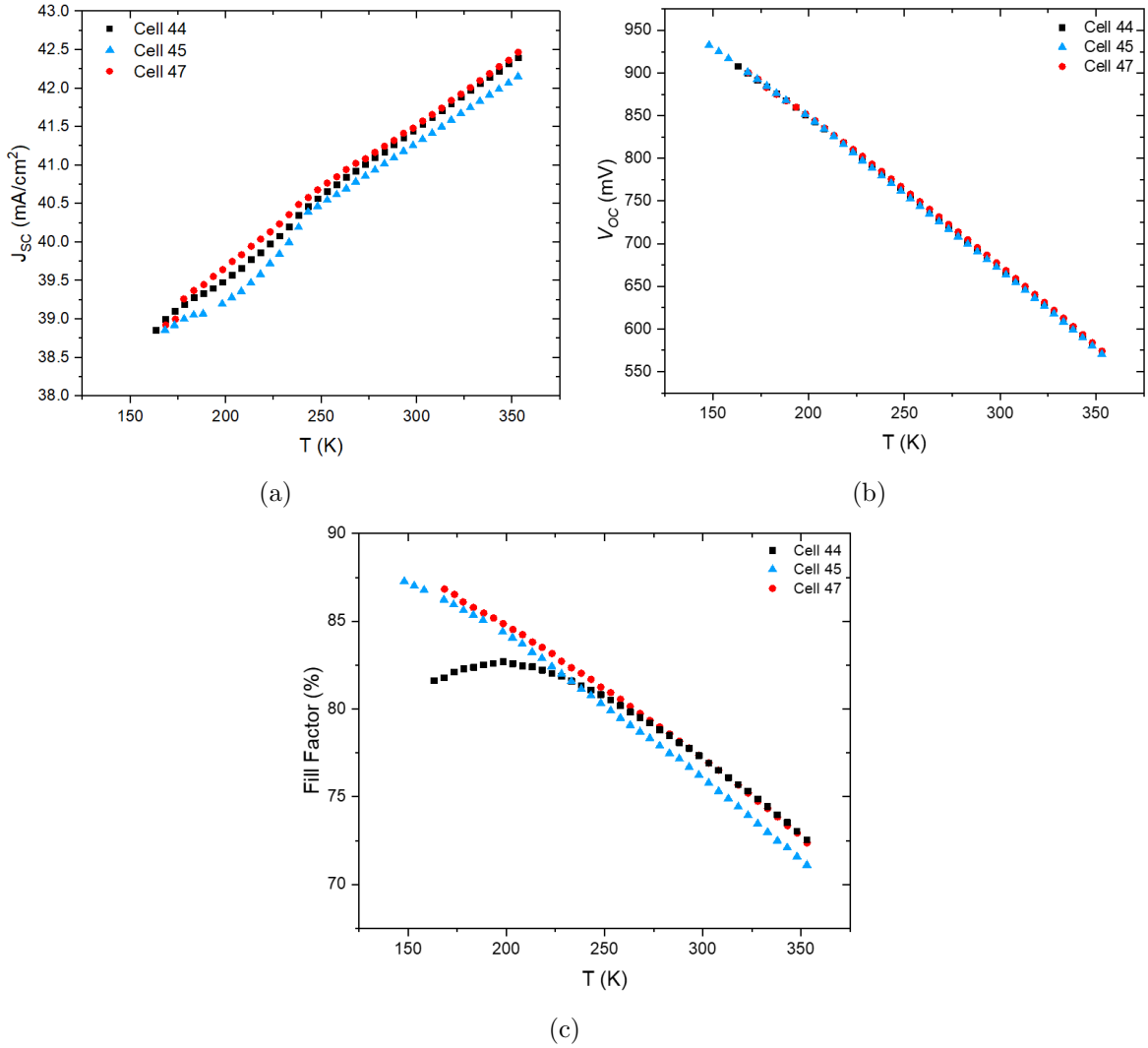

Figure 5.8: Temperature dependent data: (a) short-circuit current density, (b) open-circuit voltage, (c) fill factor.

The FF, shown in Figure 5.8(c), shows instead different behaviour in different cells. In particular, cells 45 and 47 show an increase of the FF as the temperature decreases; cell 44 shows the same behaviour only until a certain temperature, below which the FF shows a saturation and then decreases again. As explained in Section 3.2.7, the two different behaviours of the data can be modeled with two different equations for the FF:

$$FF = FF_0^*(1 - r_S) = [\nu_{oc} - ln(\nu oc + 0.72)]/(\nu_{oc} + 1) \cdot (1 - r_S) \tag{5.4}$$

which can be used to describe the behaviour exhibited by cells 45 and 47, and

$$FF = FF_0^*[1 - r_{S_1} - r_{S_2} \cdot \exp(\frac{qE_a}{kT})] \tag{5.5}$$

that introduces a parameter E_a, that represents a barrier to transport in the cells. Looking at Equations 5.4 and 5.5, it can be easily seen that the latter reduces to the former when the parameter E_a is very small, and the two series resistances r_{S_1} and r_{S_2} reduce to a single one r_S.
Therefore, it was chosen to analyse the data using only Equation 5.5, in order to study the possible differences in the parameter E_a. Figure 5.9 shows, as an example, results from the fit of cells 44 and 47 (since cells 45 and 47 have basically the same behaviour). It can be seen that the fit and the data show good agreement in both cases; the value of E_a extracted from the fit was different, being $E_a \sim 90$ meV for cell 44 and $E_a \sim 30$ meV for cell 47 (and 45).

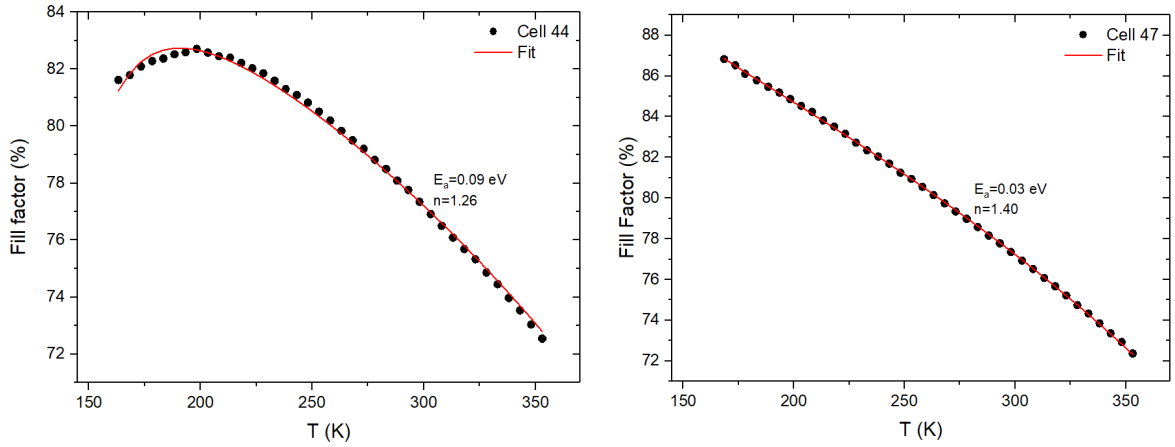

(a) (b)

Figure 5.9: Data (black dots) and fit (red line) for the FF behaviour of two cells.

The different behaviour of cell 44 can be explained, according to ref. [35], with a limitation of thermionic emission at low temperature, that can limit transport through the passivating contact. Transport limitation can be linked to the higher value of E_a shown by cell 44 with respect to the other two. In those cases, there is no barrier to transport and the cells are tunneling-dominated in the whole temperature range that was studied. At this point, it is worth noting that cell 44, that shows the saturation of the FF, contains

the passivating layer with highest boron concentration (see Table 5.2). The behaviour of this cell has therefore to be related to the different composition of the passivating layer; this will be done in the next section, where previously presented results on symmetrical samples will be compared to results obtained on solar cells.

5.3 General conclusions

The goal of the work that has just been presented was to understand how different properties of the passivating layer could influence operational parameters and transport properties of solar cells. The comparison between data from symmetrical samples and from solar cells shows some relation bewteen the two.
Data from symmetrical samples do not show any significant differences between different layers for most of the measurements, exceptions being Raman spectroscopy and optical measurements. These techniques showed a difference between samples with low (8 sccm) and high (20 sccm) TMB flux. In particular, the highly doped layer showed lower crystallinity and lower active carrier concentration with respect to the other samples. This effect could be explained by the effects of boron in the Si lattice, that makes PECVD deposition faster and therefore brings to a more amorphous layer with more defect states [39, 40].
A difference between high and low doping was also noticeable from measurements on solar cells at low temperature. The cell containing the layer with high TMB flux showed a saturation of the FF below 200 K, while the other two cells did not present this feature. This behaviour could be due to the presence of an energy barrier that limits thermionic emission at low temperature for the cell with high doping; the barrier is instead lower and therefore not visible in the other two cells. This barrier is only visible at very low temperature, outside the operational range of the solar cells, and it does not limit the performance of the device. This fact is confirmed by data measured at STC, where no significant differences could be noted between the different layers.
It has already been noted that the layer that showed lower crystallinity and active dopant concentration is the one that shows the FF saturation in the solar cell; this could be an indication that the presence of the energy barrier detected with the J-V measurements is due to the disorder created by the higher boron concentration. The density of defects created by boron is not too high, and has no consequence on transport at room temperature (as shown both by J-V measurements on cells and TLM on symmetrical samples). Defects become more important at low temperature, where they influence transport properties by limiting the fill factor.

The measurements that have been presented provide some insight into the working principles of passivating contacts and their role inside solar cells, but many points remain to be investigated. Further developement of this work could be represented by introducing other experimental techniques to study the cells (for example, EQE measurements) and also increasing the number of fabrication conditions tested both on cells and symmetrical samples.

General conclusions and perspectives

The ensemble of data collected during the work presented in this thesis shed some light on the physics underlying fired passivating contacts (FPCs).

A sistematic study of how the firing process influences transport and passivation properties of the FPCs allowed us to identify the preparation conditions that yield the best result in terms of implied open-circuit voltage and contact resistance; these properties must be optimized to obtain high efficiency cells. In particular, the influence of the firing temperature and dwell time on the crystallization of the SiC_x(p) layer in the passivating contacts, which in turn has consequences on properties such as contact resistivity or the concentration of active carriers, was investigated. Increasing the firing temperature or dwell time was observed to improve the crystallinity of the layers. On the other hand, the study showed that it is necessary to find a compromise between excellent transport properties (low contact resistivity) and the quality of the passivation of the c-Si/SiO_x interface, which controls the open circuit voltage. The V_{OC} was observed to improve with temperature/time of the firing only until a certain threshold, above which the passivation quality showed a degradation, possibly due to local disruption of the oxide stack. The investigation of changes in properties as a function of the firing conditions also led to identify the main transport mechanisms in the FPCs and clarify in what conditions they become dominant. It was found that low firing temperatures cause the presence of a barrier to charge transport across the layers, which results in thermionic field emission being the dominant transport mechanism in the contacts. This barrier becomes much lower if the layer crystallizes, allowing for pure tunneling through the c-Si/SiO_x/SiC_x junction. A comparison between experimental data and theoretical calculations also allowed to obtain quantitative values for the energetic barriers in the junction and to understand how the band diagram of these structures looks like.

Besides analyzing the consequences of changes in the firing conditions, also the composition of the layer was varied; in particular, SiC_x layers with different dopant (boron) concentrations were studied and compared. It was found that a higher concentration of boron yields negative effects on the layers by means of crystallization and activation of dopants. This study offered the occasion to compare measurements on test samples with actual solar cells containing the same layers as the symmetrical samples.
The main result was the correlation between boron concentration (linked to other properties such as crystallinity fraction of the top layer), with operational parameters of solar cells. It was found that the differences in crystallinity or dopant activation present in the test samples did not have any consequence on the operation of the cells at room temperature. However, the differences in boron concentration appeared only when measurements were carried out at low temperature. This suggested that varying the boron concentration can result in different transport mechanisms in the cells, even though the behaviour at operation conditions may be the same. These results were explained through the hypothesis of the presence of a small energetic barrier to charge transport in the band-diagram of passivating contacts with higher B concentration; being small (few meV), the barrier is not significant in the operational range of the cells, but its effects can be detected at low temperature.

Other measurements would be needed to further clarify the whole picture. More fabrication conditions have to be tested not only in test samples but also in solar cells, in order to obtain a more sistematic correlation between FPC fabrication conditions and their consequences in solar cells. Moreover, further measurements on solar cells are requested in order to better investigate the differences that were individuated at low temperature, in order to clarify if they can have any consequence at operation conditions of the cells.

Acknowledgements

This work would not have been possible without my supervisors, Prof. Daniela Cavalcoli at University of Bologna and Dr. Andrea Ingenito at PV-Lab, who guided me during the preparation of this thesis with patience and kindness.
I also would like to thank all the people at PV-Lab who helped me to handle new experimental techniques and made my stay there such a great experience; in particular I would like to thank all the people in the HTPC group for their precious help. A big thanks goes to Dr. Franz-Josef Haug, for discussing my results together and always giving really helpful suggestions, and to Frank Meyer and Philippe Wyss, who always were kind enough to find the time to give me a hand when I needed it.
At the University of Bologna, I would like to thank Dr. Maria Antonietta Fazio and Giacomo Spisni.
Finally, a special thanks to my family, friends, and the people who constantly supported me during all my study carreer.

Bibliography

[1] http://www.iea.org/publications/freepublications/publication/technology-roadmap-solar-photovoltaic-energy—2014-edition.html

[2] R.V.K Chavali et al., "Device physics underlying silicon heterojunction and passivating-contact solar cells: A topical review", *Prog Photovolt Res Appl.*, 26, pp. 241–260, 2018

[3] J. Schmidt et al., "Surface passivation of crystalline silicon solar cells: Present and future", *Sol. Energy Mater. Sol. Cells*, 187, pp. 39–54, 2018

[4] A. Richter et al., "n-Type Si solar cells with passivating electron contact: identifying sources for efficiency limitations by wafer thickness and resistivity variation", *Solar Energy Materials and Solar Cells*, 173, pp 96–105, 2017.

[5] A. Ingenito et al., "A passivating contact for silicon solar cells formed during a single firing thermal annealing," *Nature Energy*, vol. 3, no. September, pp. 800–808, 2018

[6] https://www.pveducation.org

[7] IPCC, "2014: Climate Change 2014: Synthesis Report", *Contribution of Working Groups I, II and III to the Fifth Assessment Report of the Intergovernmental Panel on Climate Change*, IPCC, Geneva, Switzerland.

[8] https://unfccc.int/process-and-meetings/the-paris-agreement/the-paris-agreement

[9] N. Armaroli et al., "Solar Electricity and Solar Fuels: Status and Perspectives in the Context of the Energy Transition", *Chemistry a European journal* 22, pp. 32-57, 2016

[10] M. Green, "Commercial progress and challenges for photovoltaics", *Nature energy*, 1, 2016

[11] T. Dittrich, "Material concepts for solar cells", *World Scientific*, 2014

[12] G. Conibeer et al. "Solar Cell Materials. Developing Technologies", *John Wiley and Sons*, Ltd., 2014.

[13] W. Shockley and H.J. Queisser, "Detailed Balance Limit of Efficiency of pn Junction Solar Cells", *Journal of Applied Physics* 32, 510, 1961

[14] M. A. Green, "Third Generation Photovoltaics. Advanced Solar Energy Conversion", *Springer*, 2003

[15] https://www.nrel.gov/pv/assets/pdfs/best-research-cell-efficiencies.20190802.pdf updated:2019

[16] L. C. Andreani et al., "Silicon solar cells: toward the efficiency limits", *Advances in Physics: X* vol. 4, no. 1, 2018

[17] https://energyeducation.ca/encyclopedia

[18] A. Hauser et al.,, "Cell and module design from the LCOE perspective", *Meyer Burger*, 2014

[19] A. Reinders et al., "Photovoltaic solar energy: from fundamentals to applications", *Wiley*, 2017

[20] P. Wurfel, "Physics of solar cells: from principles to new concepts", *Wiley*, 2005

[21] H.O. Pierson, "Handbook of Chemical Vapor Deposition: Principles, Technology and Applications", Noyes Publication, 2nd edition, 1999.

[22] https://plasma.oxinst.com/campaigns/technology/pecvd

[23] L. Kronik and Y. Shapira, "Surface photovoltage spectroscopy of semiconductor structures: at the crossroads of physics, chemistry and electrical engineering", *Surface and Interface analysis*, vol. 31, no. 10, pp. 954–965, 2001

[24] D. Cavalcoli et al., "Surface and Defect States in Semiconductors Investigated by Surface Photovoltage", *In: L. Romano et al. Semiconductors and Semimetals*, Vol. 91, no. 1, pp. 251-278, 2015

[25] T. Trupke et al., "Effective excess carrier lifetimes exceeding 100ms in float zone silicon determined from photoluminescence", Proc. 19th European Photovoltaic Solar Energy Conf., Paris, France; 2004.

[26] T. Trupke et al., "Photoluminescence Imaging for Photovoltaic Applications", *Energy Procedia*, 15, pp. 135-146, 2012

[27] R. A. Sinton et al., "Quasi-steady-state photoconductance, a new method for solar cell material and device characterization", 25th PVSC, Washington, D.C, 1996;

[28] C. V. Raman et al., "A new type of secondary radiation", *Nature*, 121, pp. 501–502, 1928

[29] M. Perani, "Nanocrystalline Silicon Based Films For Renewable Energy Applications", PhD thesis, Universitá di Bologna - Scuola di Scienze, Dottorato di Ricerca in Fisica, 2013/2014.

[30] slides by Gary Tuttle, Dept. of Electrical and Computer Engineering, Iowa State University

[31] N. Folchert et al., "Temperature-dependent contact resistance of carrier selective Poly-Si on oxide junctions", *Sol. Energy Mater. Sol. Cells*, 185, pp. 425–430, 2018

[32] D. Schroder et al., "Free carrier absorption in silicon", *IEEE Journal of solid state circuits*, vol sc-13, no. 1, 1978

[33] F-J Haug et al., "Contributions to the contact resistivity in tunnel-oxide passivating contacts", *submitted to Journal of Photovoltaics*, 2019

[34] https://www.horiba.com/material-characterization/spectroscopic-ellipsometry

[35] F. Feldmann et al., "Charge carrier transport mechanisms of passivating contacts studied by temperature-dependent J-V measurements", *Sol. Energy Mater. Sol. Cells* 178, pp. 15-19, 2018

[36] S. Eidelloth and R. Brendel, "Analytical Theory for Extracting Specific Contact Resistances of Thick Samples From the Transmission Line Method", *IEEE Electron Device Letters*, vol. 35, no. 1, pp. 9–11, 2014.

[37] G. Spisni, "Spettroscopia di fototensione superficiale di celle solari in Si con fired passivating contacts", *Physics bachelor degree thesis*, Università degli Studi di Bologna, 2019

[38] B. Terreault, "Hydrogen blistering of silicon: Progress in fundamental understanding", *Physica status solidi (a)*, 204, no. 7, pp. 2129–2184, 2007

[39] F.Fabbri et al., "Preparing the Way for Doping Wurtzite Silicon Nanowires while Retaining the Phase", *Nano Letters*, 13, pp. 5900-5906, 2013

[40] R.Saleh et al., "The influence of boron concentrations on structural properties in disorder silicon films", *Applied Surface Science*, 254, pp. 580-585, 2007

Appendix: Acronyms

Generalities on solar cells

- GHG: Greenhouse Gas
- IPCC: Intergovernmental Panel on Climate Change
- PV: PhotoVoltaics
- AM: Air Mass
- FF: Fill Factor
- STC: Standard Test Conditions
- SQ: Shockley-Queisser efficiency limit

Silicon and passivation

- LCOE: Levelized Cost Of Energy
- ARC: Anti-Reflection Coating
- BSF: Back Surface Field
- PERC: Passivated Emitter and Rear Cell
- PERL: Passivated Emitter Rear Locally diffused cell
- ETL/HTL: Electron/Hole Transport Layer
- CIS/MIS/SIS: Conductor/Metal/Semiconductor - Insulator - Semiconductor
- FPC: Fired Passivated Contacts

Experimental methods

- SE: Shiny Etched wafer
- PECVD: Plasma-Enhanced Chemical Vapour Deposition
- RTP: Rapid Thermal Processing
- ITO: Indium-Tin Oxide
- TMB: Tri-Methyl-Boron
- TLM: Transmission Line or Transfer Length Measurements
- CB/VB: Conduction/Valence Band
- SPV(SPS): Surface PhotoVoltage (Spectroscopy)
- SCR: Space Charge Region
- PL(EL): Photo(Electro)Luminescence
- QSSPC: Quasi-Steady State PhotoConductance
- FTIR: Fourier Transform InfraRed spectroscopy
- FCA: Free Carrier Absorption